

JGR Solid Earth

RESEARCH ARTICLE

10.1029/2020JB019852

Key Points:

- New GPS data show that postseismic deformation of the 2015 M_w 7.8 Gorkha (Nepal) earthquake extended far northward into southern Tibet
- Kinematic and dynamic models suggest that the northward reach of deformation likely reflects the influence of viscoelastic relaxation
- Afterslip likely dominated postseismic deformation in the near field, transferring stress back to the (relocked) Gorkha rupture zone

Supporting Information:

- Supporting Information S1

Correspondence to:

C. Rollins,
j.c.rollins@leeds.ac.uk

Citation:




Liu-Zeng, J., Zhang, Z., Rollins, C., Gualandi, A., Avouac, J.-P., Shi, H., et al. (2020). Postseismic deformation following the 2015 M_w 7.8 Gorkha (Nepal) earthquake: New GPS data, kinematic and dynamic models, and the roles of afterslip and viscoelastic relaxation. *Journal of Geophysical Research: Solid Earth*, 125, e2020JB019852. <https://doi.org/10.1029/2020JB019852>

Received 25 MAR 2020

Accepted 29 JUN 2020

Accepted article online 8 JUL 2020

Postseismic Deformation Following the 2015 M_w 7.8 Gorkha (Nepal) Earthquake: New GPS Data, Kinematic and Dynamic Models, and the Roles of Afterslip and Viscoelastic Relaxation

J. Liu-Zeng^{1,2}, Z. Zhang³, C. Rollins^{4,5} , A. Gualandi^{5,6} , J.-P. Avouac⁵ , H. Shi⁷, P. Wang¹, W. Chen⁸, R. Zhang⁷, P. Zhang¹, W. Wang¹, Y. Li⁷, T. Wang⁷, and Z. Li¹

¹State Key Laboratory of Earthquake Dynamics, Institute of Geology, China Earthquake Administration, Beijing, China,

²Institute of Surface Earth System Science, Tianjin University, Tianjin, China, ³Institute of Tibetan Plateau Research, Chinese Academy of Sciences, Beijing, China, ⁴School of Earth and Environment, University of Leeds, Leeds, UK,

⁵Division of Geological and Planetary Sciences, California Institute of Technology, Pasadena, CA, USA, ⁶Jet Propulsion Laboratory, California Institute of Technology, Pasadena, CA, USA, ⁷China Earthquake Networks Center, Beijing, China,

⁸Department Research Center of China Earthquake Administration, Beijing, China

Abstract We report Global Positioning System (GPS) measurements of postseismic deformation following the 2015 M_w 7.8 Gorkha (Nepal) earthquake, including previously unpublished data from 13 continuous GPS stations installed in southern Tibet shortly after the earthquake. We use variational Bayesian Independent Component Analysis (vbICA) to extract the signal of postseismic deformation from the GPS time series, revealing a broad displacement field extending >150 km northward from the rupture. Kinematic inversions and dynamic forward models show that these displacements could have been produced solely by afterslip on the Main Himalayan Thrust (MHT) but would require a broad distribution of afterslip extending similarly far north. This would require the constitutive parameter $(a - b)\sigma$ to decrease northward on the MHT to ≤ 0.05 MPa (an extreme sensitivity of creep rate to stress change) and seems unlikely in light of the low interseismic coupling and high midcrustal temperatures beneath southern Tibet. We conclude that the northward reach of postseismic deformation more likely results from distributed viscoelastic relaxation, possibly in a midcrustal shear zone extending northward from the seismogenic MHT. Assuming a shear zone 5–20 km thick, we estimate an effective shear-zone viscosity of $\sim 3 \cdot 10^{16}$ – $3 \cdot 10^{17}$ Pa·s over the first 1.12 postseismic years. Near-field deformation can be more plausibly explained by afterslip itself and implies $(a - b)\sigma \sim 0.5$ – 1 MPa, consistent with other afterslip studies. This near-field afterslip by itself would have re-increased the Coulomb stress by ≥ 0.05 MPa over >30% of the Gorkha rupture zone in the first postseismic year, and deformation further north would have compounded this reloading.

1. Introduction

The 25 April 2015 M_w 7.8 Gorkha (Nepal) earthquake ruptured the lower (northern) edge of the interseismically locked portion of the Main Himalayan Thrust (MHT) just north of Kathmandu (Figure 1) (e.g., Avouac et al., 2015; Galetzka et al., 2015). The Gorkha earthquake imparted substantial stress changes both to the surrounding locked portion of the MHT and to its northward extension beneath the Himalaya and Tibet (Figure 2), on which deformation likely occurs aseismically (Figure 1a) as distributed shear and/or brittle fault creep (e.g., Ader et al., 2012; Cattin & Avouac, 2000). These northward stress changes induced transient postseismic deformation that was detectable in geodetic data (e.g., Wang & Fialko, 2018; Zhao et al., 2017). This postseismic deformation can provide insight into the rheology of the crust beneath the Himalaya and Tibet, which is crucial to understand particularly as this northward extension in turn assists in the stress loading of the seismogenic MHT to the south.

However, the data used in previous studies of post-Gorkha deformation provided limited resolution of this key region north of the rupture: Global Positioning System (GPS) data (Figures 1a and 1b, open squares) were either confined to Nepal (Gualandi et al., 2017; Ingleby et al., 2020; Jouanne et al., 2019; Wang &

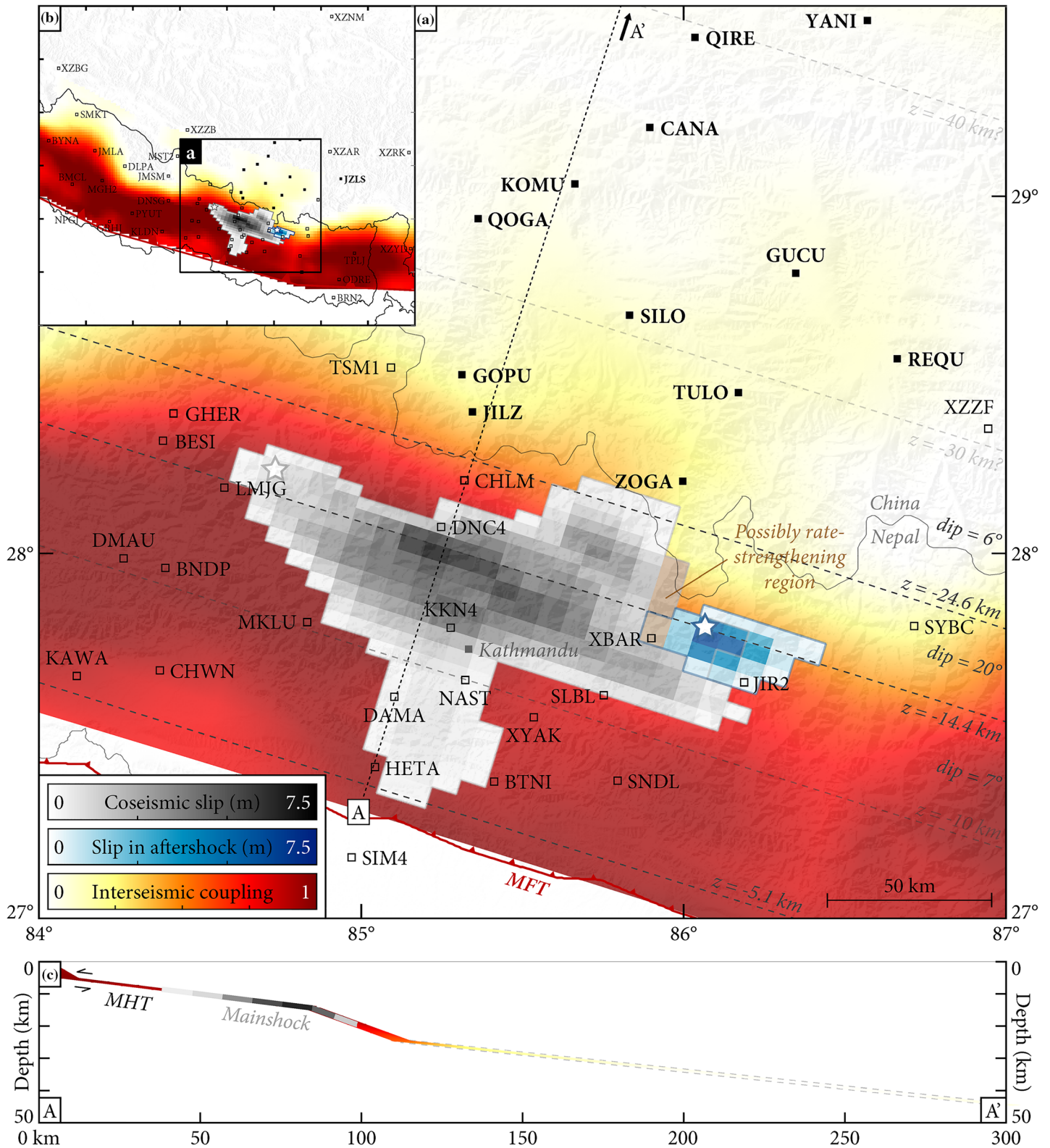


Figure 1. (a) The Gorkha earthquake and distribution of GPS stations in Nepal and Tibet. Color shading: Interseismic coupling on the MHT (Stevens & Avouac, 2015). Gray/blue stars, patches, and outlines: Epicenters, Elliott et al. (2016) slip distributions, and ≥ 0.25 -m-slip areas of the mainshock/ $M_w = 7.3$ aftershock. Brown area: Possible stable-sliding region in between. Empty/filled squares: Previously published/unpublished stations. (b) Regional tectonic setting and GPS network. (c) Cross section of MHT geometry extended from Elliott et al. (2016), colored by coupling coefficient.

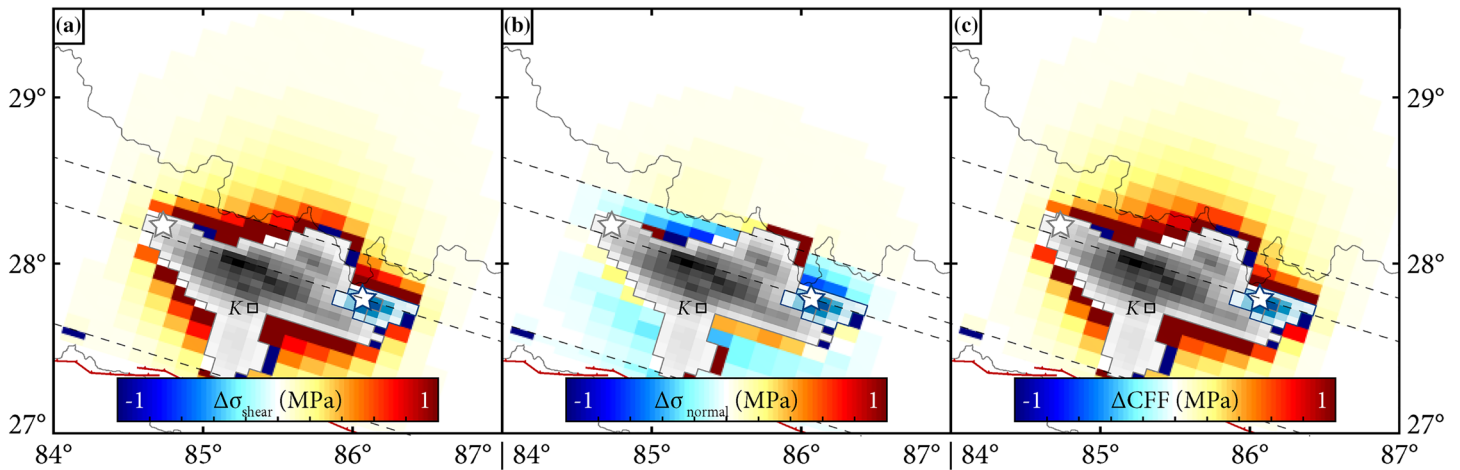


Figure 2. (a) Shear, (b) normal, and (c) Coulomb stress changes imparted to the surrounding MHT by the mainshock and $M_w7.3$ aftershock, calculated using the Elliott et al. (2016) source models for both. Here and throughout this study, Coulomb stress changes are computed assuming an effective friction of 0.6. K = Kathmandu.

Fialko, 2018) or located hundreds of km from the rupture in Tibet (Jiang et al., 2018; Tian et al., 2020; Zhao et al., 2017), and Interferometric Synthetic Aperture Radar (InSAR) coverage was inhibited by atmospheric interference over the Himalaya (Ingleby et al., 2020; Wang & Fialko, 2018). In part due to this limited resolution, these studies reached varied conclusions about what this postseismic deformation to the north actually entailed: Some inferred or assumed that frictional afterslip was the dominant deformation process (Gualandi et al., 2017; Ingleby et al., 2020; Jiang et al., 2018; Jouanne et al., 2019; Sreejith et al., 2016; Wang & Fialko, 2018), while others inferred a combination of afterslip and distributed viscoelastic relaxation (Jouanne et al., 2019; Tian et al., 2020; Zhao et al., 2017). Here we present previously unpublished data from 13 continuous GPS stations installed within ~ 250 km of the rupture in southern Tibet shortly after the earthquake (Figures 1a and 1b, filled squares) and use these data to place sharper constraints on the rheology of the Himalaya and Tibet.

2. Data Processing and Postseismic Signal Extraction

We process and prepare the data in a multi-step procedure as follows (Figures 3–7).

1. We process raw GPS data from the 13 new stations along with 14 other stations in Tibet operated by the Crustal Movement Observation Network of China (CMONOC), 37 regional UNAVCO stations, and 828 IGS worldwide stations. We use GAMIT/GLOBK (Herring et al., 2015) to produce daily position time series in ITRF2008 (Supporting Information S1; Figures 3 and 4, light gray) (Altamimi et al., 2011). The data set as a whole span from January 2010 to June 2016, with temporal coverage varying from station to station. We use the data from stations within 1,000 km of the mainshock epicenter and add time series from the Nevada Geodetic Laboratory (NGL) (Blewitt et al., 2018) at stations within this radius that are not included in the processed set, yielding a total of 168 stations (Figures 1a and 1b, squares) including the 13 in southern Tibet (filled squares). The GAMIT/GLOBK-processed and NGL time series are comparable within uncertainties at stations included in both data sets (see Data Availability Statement, #4).
2. We convert these ITRF2008 time series to a fixed-India reference frame. The time series contain signals from steady interseismic motion (e.g., Ader et al., 2012), seasonal oscillations (Bettinelli et al., 2008), offsets from station maintenance, coseismic and postseismic deformation of the 2011 $M_w6.9$ Sikkim earthquake (Chopra et al., 2014), coseismic offsets from the Gorkha earthquake and the $M_w7.3$ aftershock of 12 May 2015 (Figure 1a, blue), and finally, the signal of post-Gorkha deformation. To estimate any of these signals in any time period with minimal bias requires estimating all of the signals present in that time period. To convert to a fixed-India reference frame specifically

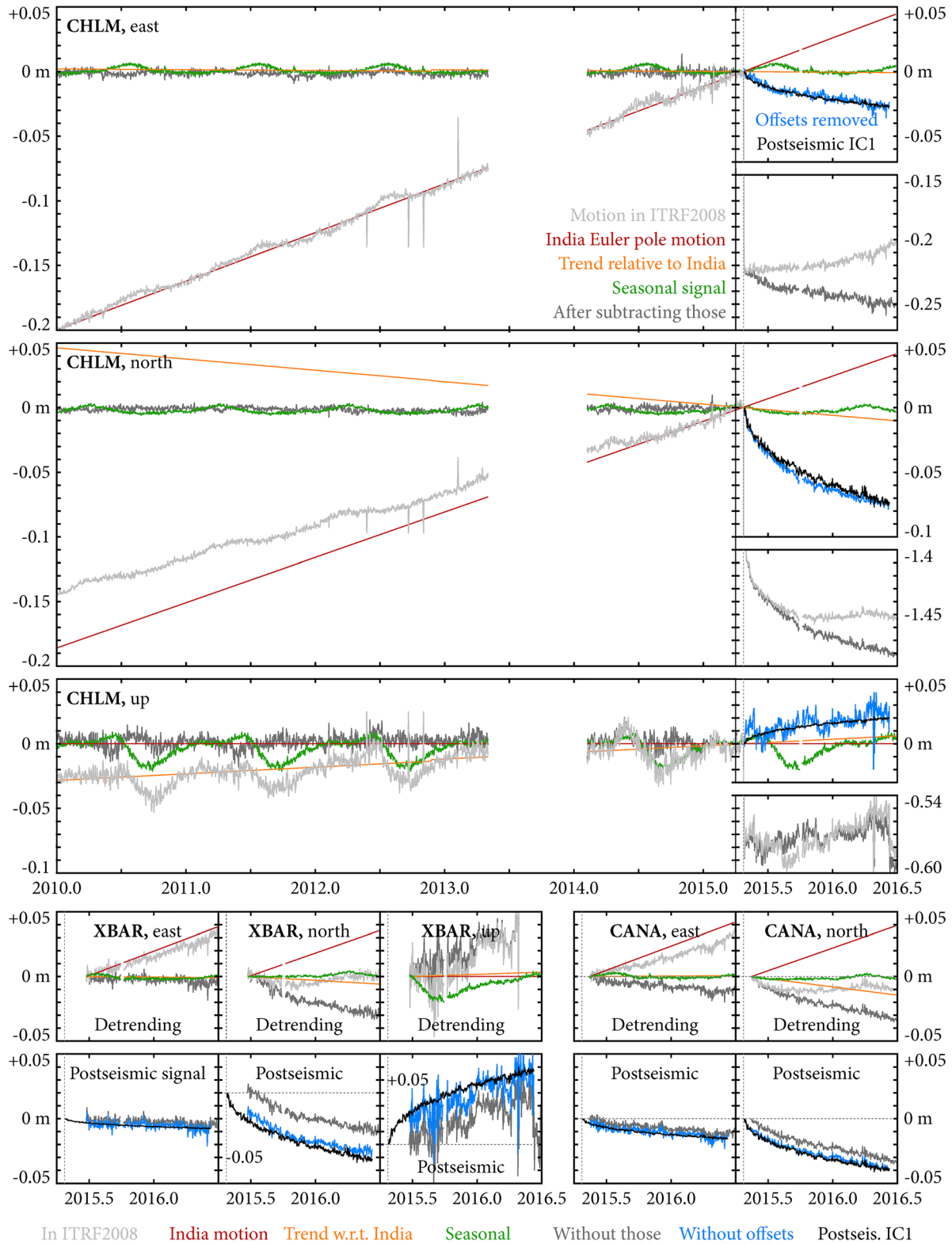


Figure 3. Decomposition of GPS time series (section 2) for stations CHLM and XBAR in Nepal and CANA in Tibet. Vertical dashed lines show the time of the Gorkha earthquake (2015.31). (XBAR and CANA began recording in mid-2015.)

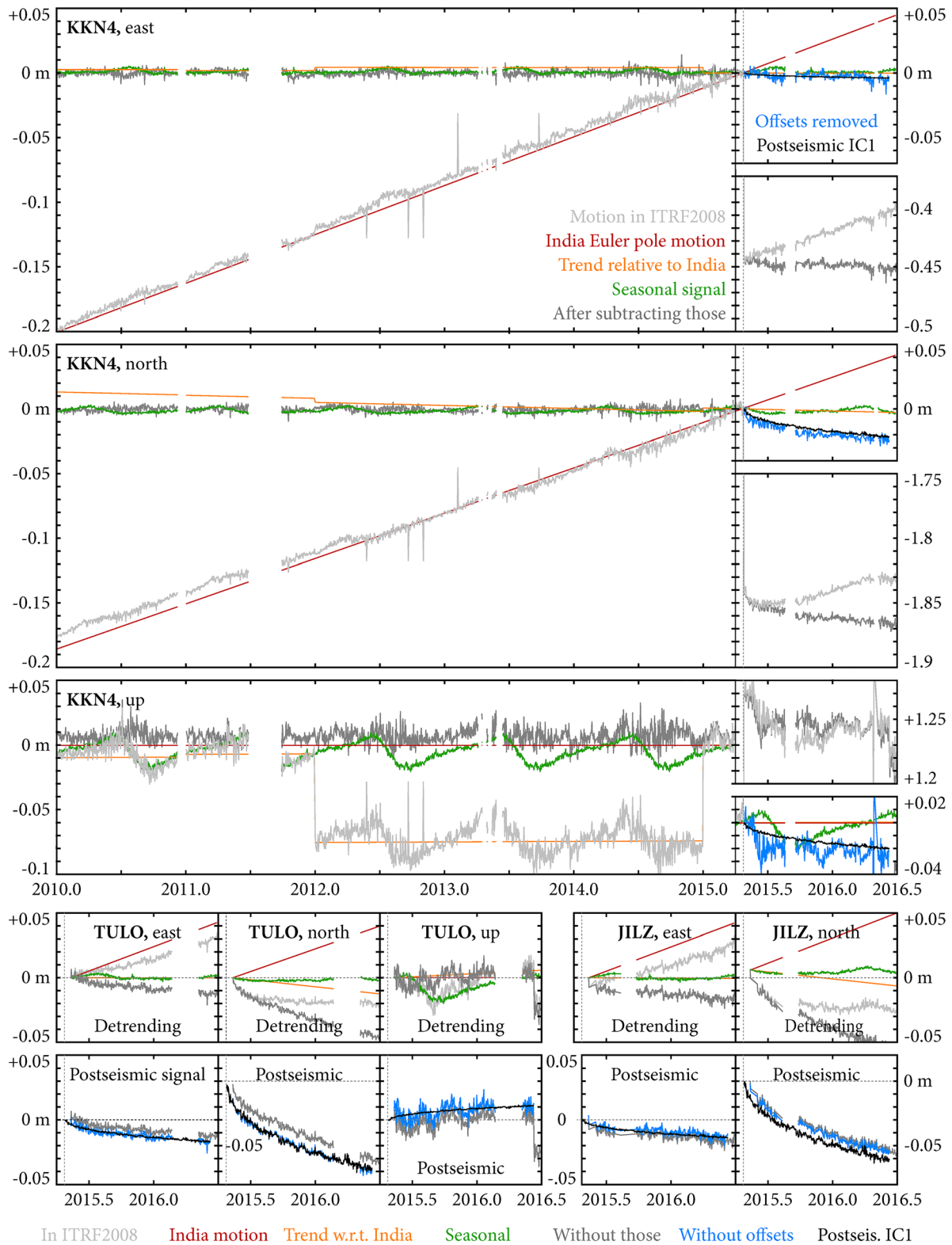


Figure 4. Decomposition of GPS time series (section 2) for station KKN4 in Nepal and TULO and JILZ in Tibet. (TULO and JILZ began recording in mid-2015.)

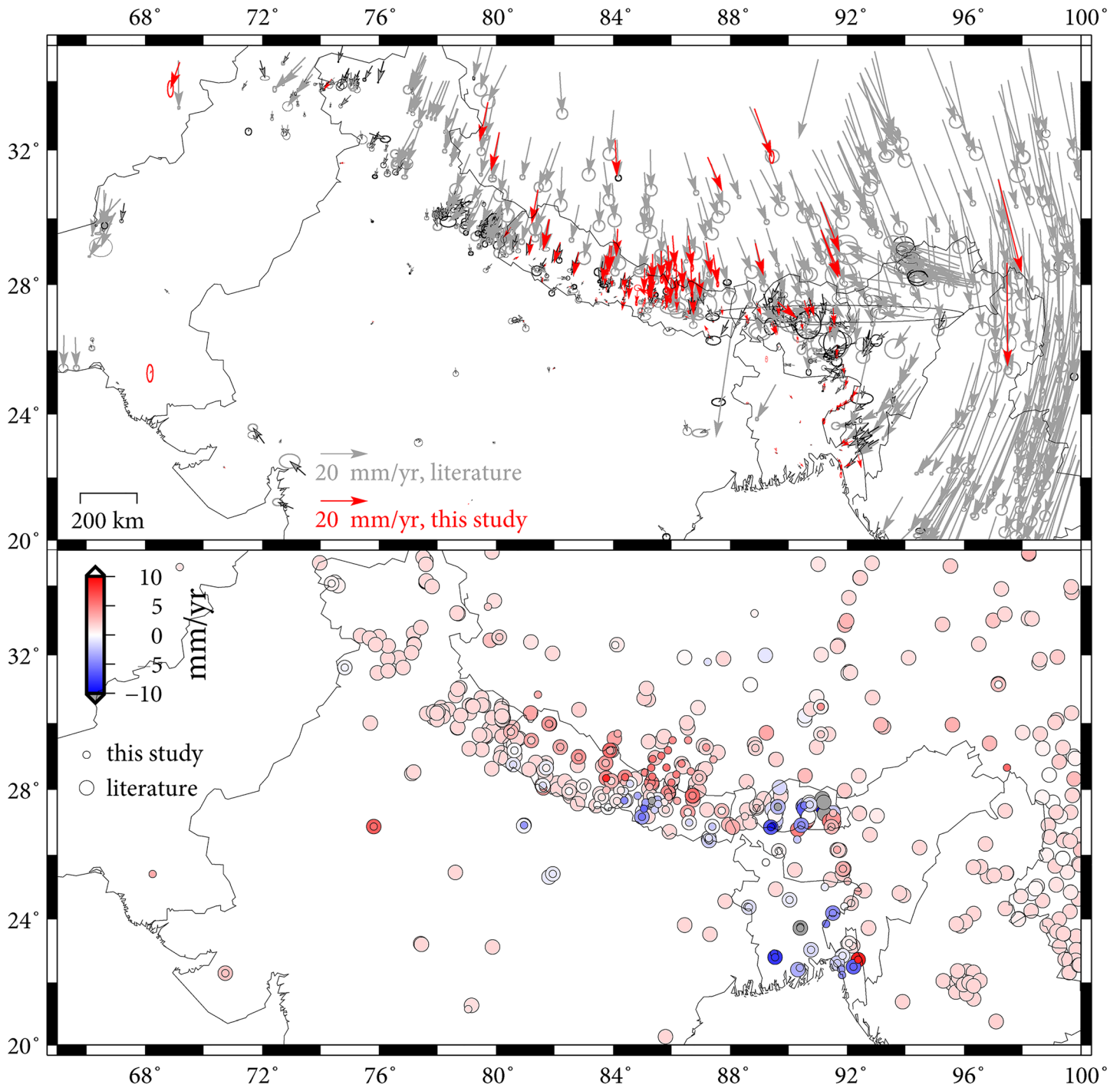


Figure 5. GPS station velocities relative to fixed India. Black arrows (top) and large circles (bottom) indicate horizontal and vertical interseismic velocities from literature (section 2). Red arrows (top) and small circles (bottom) indicate horizontal and vertical interseismic velocities at the continuous GPS stations considered in this study (orange lines in Figures 3 and 4). At stations with ≥ 1 yr of pre-Gorkha we calculate the velocities from trajectory models; at the remaining stations we interpolate from these velocities by kriging (section 2).

requires estimating (and removing) the signals of steady Indian plate motion within ITRF2008. To do so, we fit the pre-Gorkha-earthquake portions of continuous NGL time series at stations located on stable India (north, east, and up components separately) to “trajectory” models (e.g., Bevis & Brown, 2014),

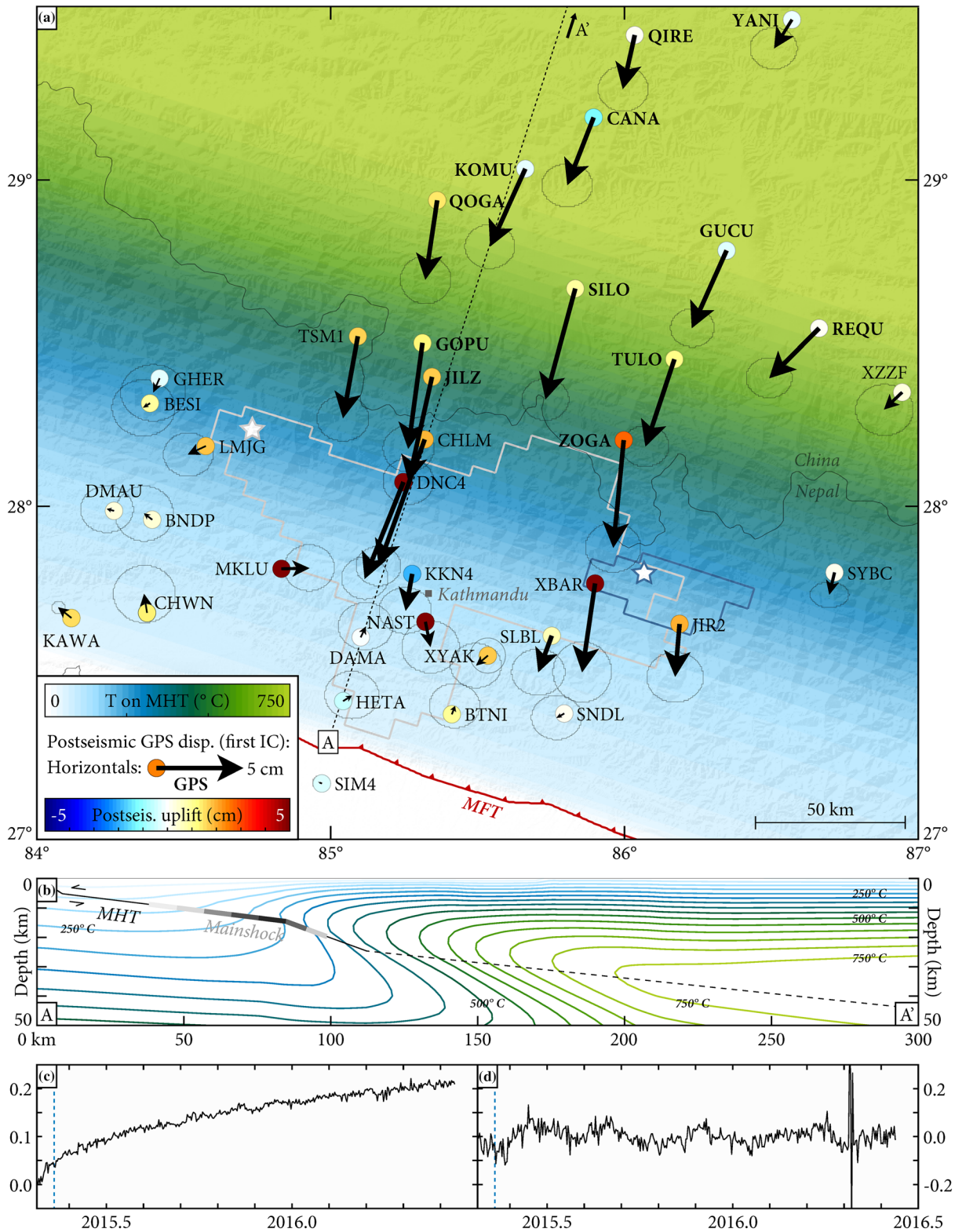


Figure 6. (a) Cumulative 1.12-yr postseismic GPS displacements (filled circles and black arrows) from the first postseismic Independent Component (IC) after correcting for other signals (section 2). Black ellipses: One-sigma uncertainties in cumulative horizontals. Color shading: Estimated temperature along the MHT from averaging the thermal models of Henry et al. (1997) and Herman et al. (2010) and interpolating onto the Elliott et al. (2016) MHT geometry. Gray/blue stars and outlines: Epicenters and ≥ 0.25 -m-slip areas of the mainshock/ $M_w 7.3$ aftershock. Bold text indicates new stations. (b) Cross section of MHT geometry and estimated temperature. (c, d) Non-dimensionalized and normalized temporal functions of the first two postseismic ICs (of which we only use the first). Blue dashed lines: Time of the $M_w 7.3$ aftershock.

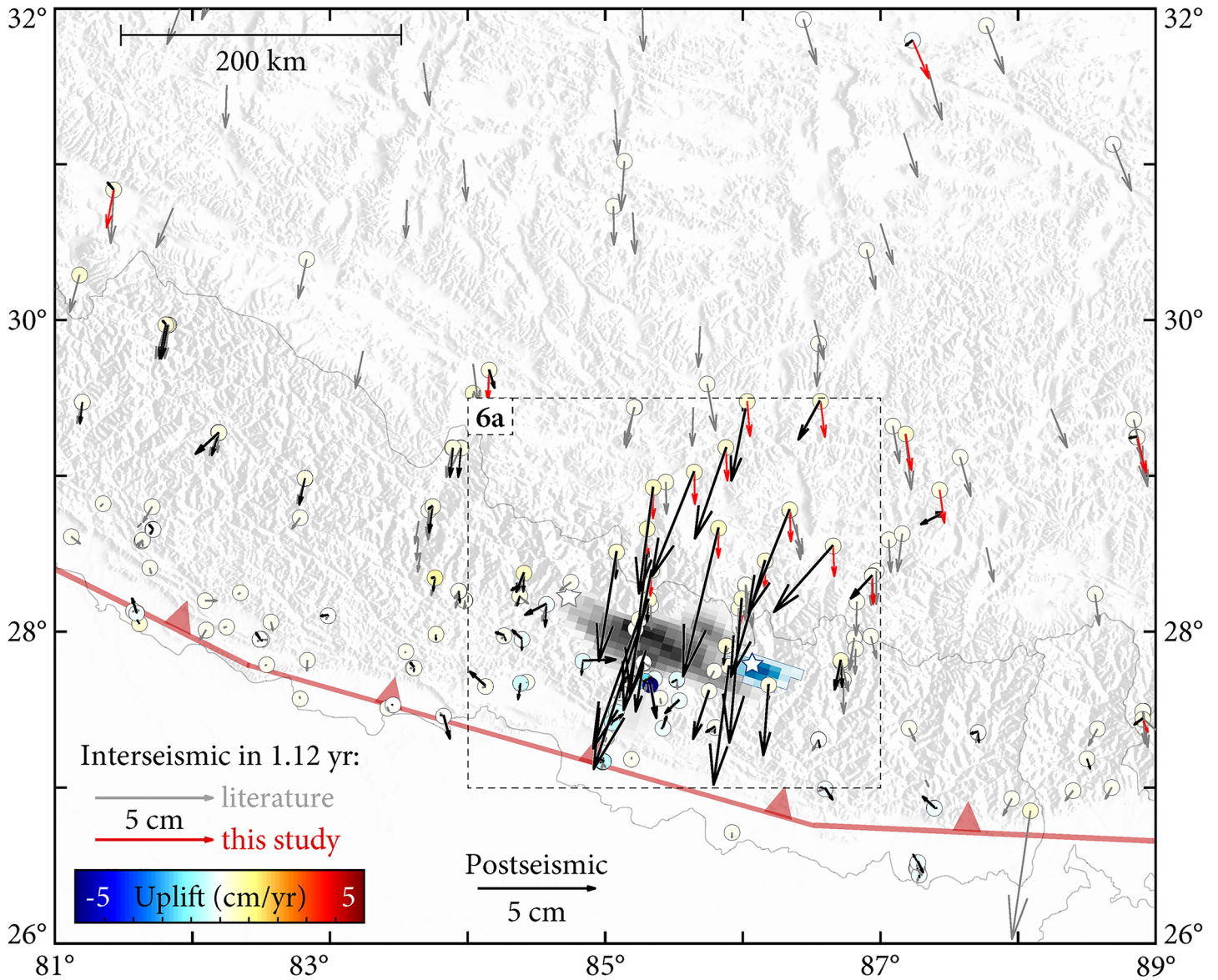


Figure 7. Cumulative 1.12-yr horizontal postseismic displacements (black arrows), displacements over 1.12 yr from interpolated horizontal interseismic velocities used in this study (red arrows), and displacements over 1.12 yr from horizontal interseismic velocities from literature (gray arrows). Colored circles: Interseismic vertical velocities (yr^{-1}). Inner rectangle indicates area covered by Figures 6a (and 1a).

$$x(t) = m_1 + m_2 t + m_3 \sin(2\pi t) + m_4 \cos(2\pi t) + m_5 \sin(4\pi t) + m_6 \cos(4\pi t) + m_7 H(t - t_{SK}) + m_8 H(t - t_{SK}) \left(1 - \exp\left(-\frac{t - t_{SK}}{m_9}\right) \right) + \sum m_i H(t - t_i), \quad (1)$$

in which m_1 is a reference position, m_2 is a secular (interseismic) velocity, m_3 and m_4 are coefficients of an annual oscillation, m_5 and m_6 are coefficients of a semiannual oscillation, m_7 is the amplitude of a Heaviside step function representing the coseismic offset in the 2011 Sikkim earthquake, m_8 is the amplitude of postseismic deformation of the Sikkim earthquake with characteristic time m_9 , and m_i are the amplitudes of Heaviside functions representing offsets from other earthquakes and station maintenance. We take the estimated horizontal secular velocities at these stations, merge these with nearby GPS velocities (in ITRF2008) from literature (Ader et al., 2012; Banerjee & Bürgmann, 2002; Bettinelli et al., 2006; Calais et al., 2006; Chlieh et al., 2008; Duong et al., 2006; Gahalaut et al., 2013; Gan et al., 2007; Gupta et al., 2015; He et al., 2013; Hsu et al., 2009; Ischuk et al., 2013; Jade, 2004; Jade

- et al., 2007, 2011, 2014; Jouanne et al., 2014; Jouanne et al., 2017; Kundu et al., 2014; Liang et al., 2013; Mahesh et al., 2012; Marechal et al., 2016; Maurin et al., 2010; Mohadjer et al., 2010; Mukul et al., 2010; Ponraj et al., 2011; Schiffman et al., 2013; Simons et al., 2007; Socquet et al., 2006; Steckler et al., 2016; Szeliga et al., 2012; Tang et al., 2010; Wang et al., 2014; Yang et al., 2008; Zubovich et al., 2010), and fit the merged velocity field to a model of rotation about an Euler pole using a least squares method (Ader et al., 2012). The best fitting pole is at $51.72 \pm 0.01^\circ\text{N}$, $1.33 \pm 0.06^\circ\text{E}$ and has angular velocity $0.5118 \pm 0.0002^\circ/\text{Myr}$. We then subtract the predicted linear trends from this rotation (Figures 3 and 4, red) from the time series of all 168 stations, yielding position time series relative to fixed India.
3. We next remove India-relative interseismic motion from the time series. At stations with at least 1 yr of pre-Gorkha data (69 total), we fit the pre-Gorkha portions of the India-relative time series to a new set of trajectory models with the same terms. We spatially interpolate the estimated velocities to the other 99 stations by kriging (Gualandi et al., 2017). Figure 5 shows that the interpolated India-relative velocities (red arrows and small circles) compare well with India-relative velocities at nearby stations from the literature (black arrows and large circles). We detrend all time series by subtracting the linear trends (Figures 3 and 4, orange) of the interpolated India-relative motions and also remove (pre-Gorkha) offsets estimated from this second set of trajectory models.
 4. We next characterize and remove seasonal deformation. We select the pre-Gorkha portions of the detrended time series at the 30 stations that have coverage over at least 50% of the pre-Gorkha time period. Rather than using a trajectory model with sinusoids, which would assume a perfect regularity to seasonal oscillations, we estimate these signals by applying variational Bayesian Independent Component Analysis (vbICA) (Choudrey & Roberts, 2003; Gualandi et al., 2016, 2017), which has been used successfully in previous studies of seasonal strain in the Himalaya (Larochelle et al., 2018). This method divides the time series into a limited number of Independent Components (ICs), each characterized by a temporal function V_i that is statistically independent of the temporal functions of other ICs, and characterized by a spatial distribution U_i and weighted by a factor S_i such that

$$X \approx USV^T, \quad (2)$$

where X is the set of detrended and centered (i.e., with zero mean) time series at these 30 stations. Five ICs are extracted (Figure S1), and frequency analysis of their temporal functions (Figure S2) shows that four of them describe seasonal deformation and the fifth likely describes the postseismic deformation of the 2011 Sikkim earthquake.

5. We project each of the four seasonal ICs' temporal functions forward in time by computing their sample mean and variance on each day of the year in the pre-Gorkha period and assuming that the same mean and variance apply on that day of the year in the post-Gorkha period. We interpolate the spatial mappings U of these four ICs to all 168 stations (Gualandi et al., 2017) and multiply the interpolated U , the weights S , and these forward-projected functions V to yield estimated seasonal motions at all stations over the 2010–2016 period (Figures 3 and 4, green). We then subtract these from the time series (Figures 3 and 4, dark gray).
6. We then correct the post-Gorkha portions of these time series for the $M_w 7.3$ aftershock of 12 May 2015 and other post-Gorkha instrumental offsets by subtracting the difference between the positions on the day after and before each offset (Figures 3 and 4, blue).
7. Finally, to better isolate the postseismic signals from seasonal deformation, we perform a second vbICA on these corrected post-Gorkha time series at the 67 stations that have data over $\geq 20\%$ of the postseismic period. (Ingleby et al., 2020, similarly performed a second decomposition to remove residual seasonal motion.) The first IC from this second vbICA (weight 1,273 mm), referred to hereafter as the “first postseismic IC,” explains $\sim 60\%$ of the data variance of the corrected time series, and its temporal function has the characteristic decaying form of postseismic deformation (Figure 6c). We interpret the second postseismic IC (weight 997 mm) as representing residual seasonal motion (Figure 6d).

The final “data set” thus consists of the first postseismic IC at the 67 stations with data over $\geq 20\%$ of the 1.12-yr postseismic period (Figures 3 and 4, black). It reveals a broad deformation field extending northward from the rupture into Tibet (Figures 6a and 7), featuring mainly south-southwest horizontal motion and decaying northward. Cumulative 1.12-yr postseismic displacements decrease from >7 cm horizontal and >5 cm vertical motion just north of the rupture to <2 cm horizontal motion and minimal vertical motion ~ 150 km to

the north. The 1.12-yr postseismic displacements dwarf the interseismic motions that would be expected over 1.12 yr in the epicentral area (Figure 7).

3. Kinematic (Inverse) Modeling of Afterslip

To test whether post-Gorkha deformation may have been dominantly produced by afterslip (Gualandi et al., 2017; Ingleby et al., 2020; Jiang et al., 2018; Sreejith et al., 2016; Wang & Fialko, 2018), we invert the spatial distribution U of the first postseismic IC to derive a kinematic model of afterslip on the MHT. We use the ramp-flat-ramp-flat geometry for the MHT from Elliott et al. (2016), extended ~ 200 km further downdip and further along strike in each direction (Figures 1a and 1c), similar to Jiang et al. (2018). We adapt the PCAIM linear inversion procedure (Kositsky & Avouac, 2010) for the use of vbICA and use the regularization method of Radiguet et al. (2011), where the a priori model covariance between subdivided patches decreases exponentially with distance.

Figure 8a shows our preferred kinematic afterslip model, in which both dip slip and strike slip are allowed and unbounded, as in Gualandi et al. (2017). It shows that the broad postseismic deformation field can be fit to afterslip provided that the afterslip extended >100 km north of the coseismic rupture on the lower flat of the MHT (Figure 8b). This result is also seen in models that constrain the slip rake or use a planar MHT geometry (Figure S3). The preferred model also features substantial afterslip on the lower ramp just north of the rupture and on a section between the mainshock and largest aftershock that likely did not slip in either event (brown dashed region) and has been postulated to have a stable-sliding rheology (e.g., Ader et al., 2012; Lindsey et al., 2015). We infer some possible overlap between coseismic and postseismic slip at the lower edge of the coseismic rupture (Figure 8a), and minimal deformation updip, west and east of the rupture, consistent with Wang and Fialko (2018) and Zhao et al. (2017). Some shallow strike-slip afterslip is inferred from the vertical motions at KKN4, NAST, and MKLU and the eastward motion at MKLU, but this slip is likely not real (Supporting Information S1).

4. Implications for Fault Friction

We use the preferred kinematic afterslip model and the theory of steady-state frictional sliding to estimate the frictional properties on the MHT. The constitutive parameter $a - b = \frac{\partial \mu_{ss}}{\partial \ln(v)}$ quantifies the sensitivity of the steady-state friction coefficient μ_{ss} to the sliding rate v . Here a and b are frictional parameters; $a > b$ denotes a rate-strengthening rheology favoring stable creep, and $a < b$ denotes a rate-weakening rheology allowing slip to become unstable and seismic. Note that only the product $(a - b)\sigma$, where σ is the effective normal stress, can be estimated using afterslip observations (Perfettini & Avouac, 2004). Similar analyses have been conducted for post-Gorkha deformation by Wang and Fialko (2018), Ingleby et al. (2020), and Tian et al. (2020), who refer to $(a - b)\sigma$ as $a\sigma$, and by Jouanne et al. (2019), who refers to it as $(a - b)\sigma$ as we do here.

We estimate $(a - b)\sigma$ in two complementary ways. The first approach (Figure 9c) compares the initial acceleration in creep rates to the coseismic stress changes that induced it. We quantify the initial acceleration on each patch of the fault as $d = \frac{V_+}{V_C}$ (Figure 9b), where V_C is the interseismic creep rate and V_+ is the sliding velocity immediately after the earthquake, and we estimate this ratio from the spatiotemporal evolution of the first postseismic IC (Figure 6c). Then, following Perfettini and Avouac (2004),

$$(a - b)\sigma = \frac{\Delta CFF}{\ln d}, \quad (3)$$

where ΔCFF is the coseismic Coulomb stress change, which we calculate (Figure 2c) using the Elliott et al. (2016) slip models for the Gorkha earthquake and the $M_w 7.3$ aftershock.

The second approach (Figure 9f) estimates the frictional properties from how the afterslip rates decayed over time, which we quantify using t_r , the relaxation time of each patch, as in Gualandi et al. (2017) (Figure 9e). Then, following Perfettini and Avouac (2004, 2007),

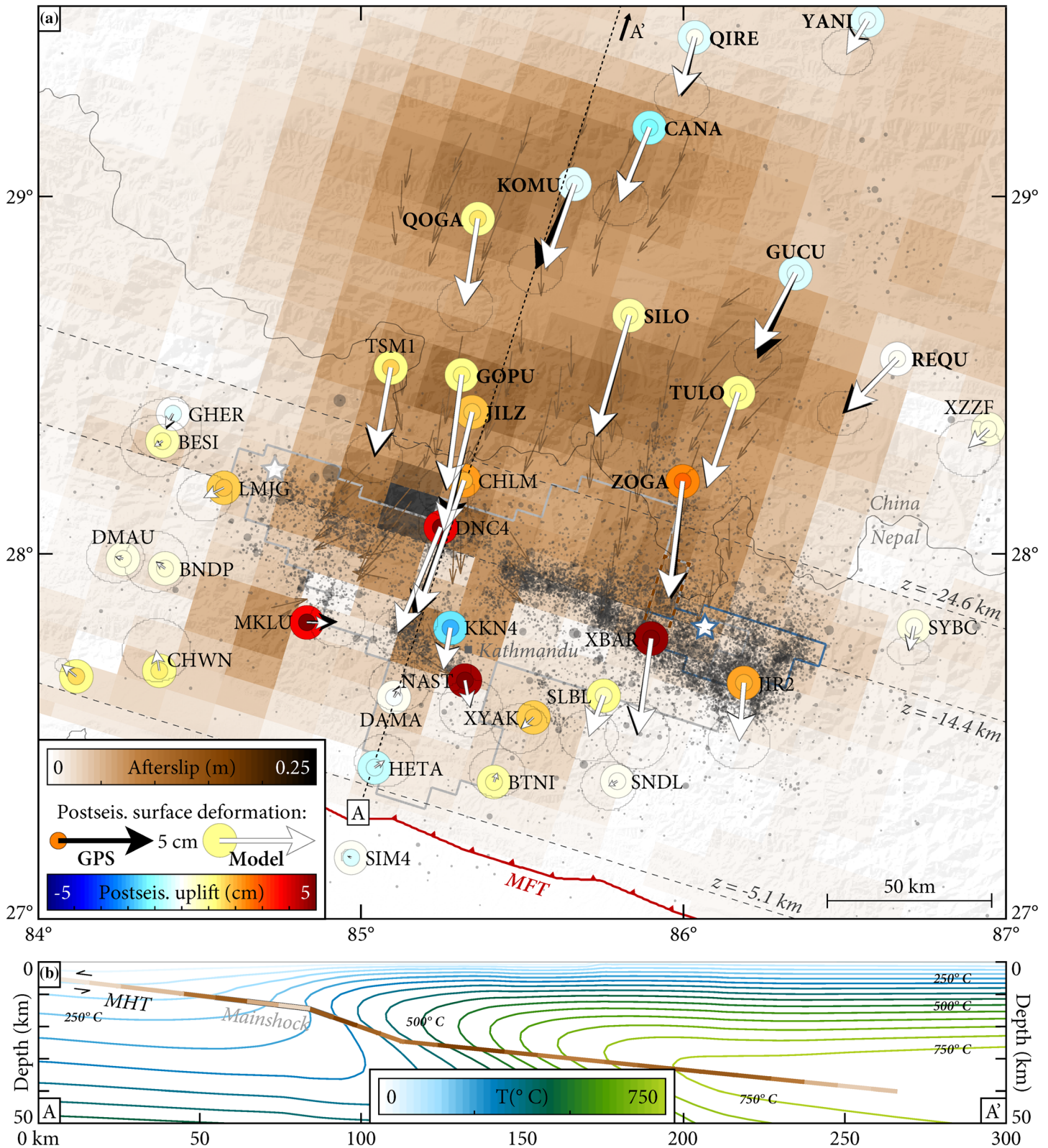


Figure 8. Preferred kinematic afterslip model (section 3). (a) Cumulative 1.12-yr afterslip (brown patches) and displacements. Brown arrows: Slip vectors for patches with >9 cm slip (maximum slip is 26 cm). Black and white arrows: Observed and predicted horizontal displacements. Small/large colored circles: Observed/predicted vertical displacements. Gray/blue stars and outlines: Epicenters and ≥ 0.25 -m-slip areas of the mainshock/ $M_w 7.3$ aftershock. Dashed brown region: Possible stable-sliding region in between. Gray filled circles: $M \geq 3$ aftershocks through May 2016 (Baillard et al., 2017; Yamada et al., 2020). (b) Cross section of afterslip magnitude along profile A-A', overlaid on estimated temperature.

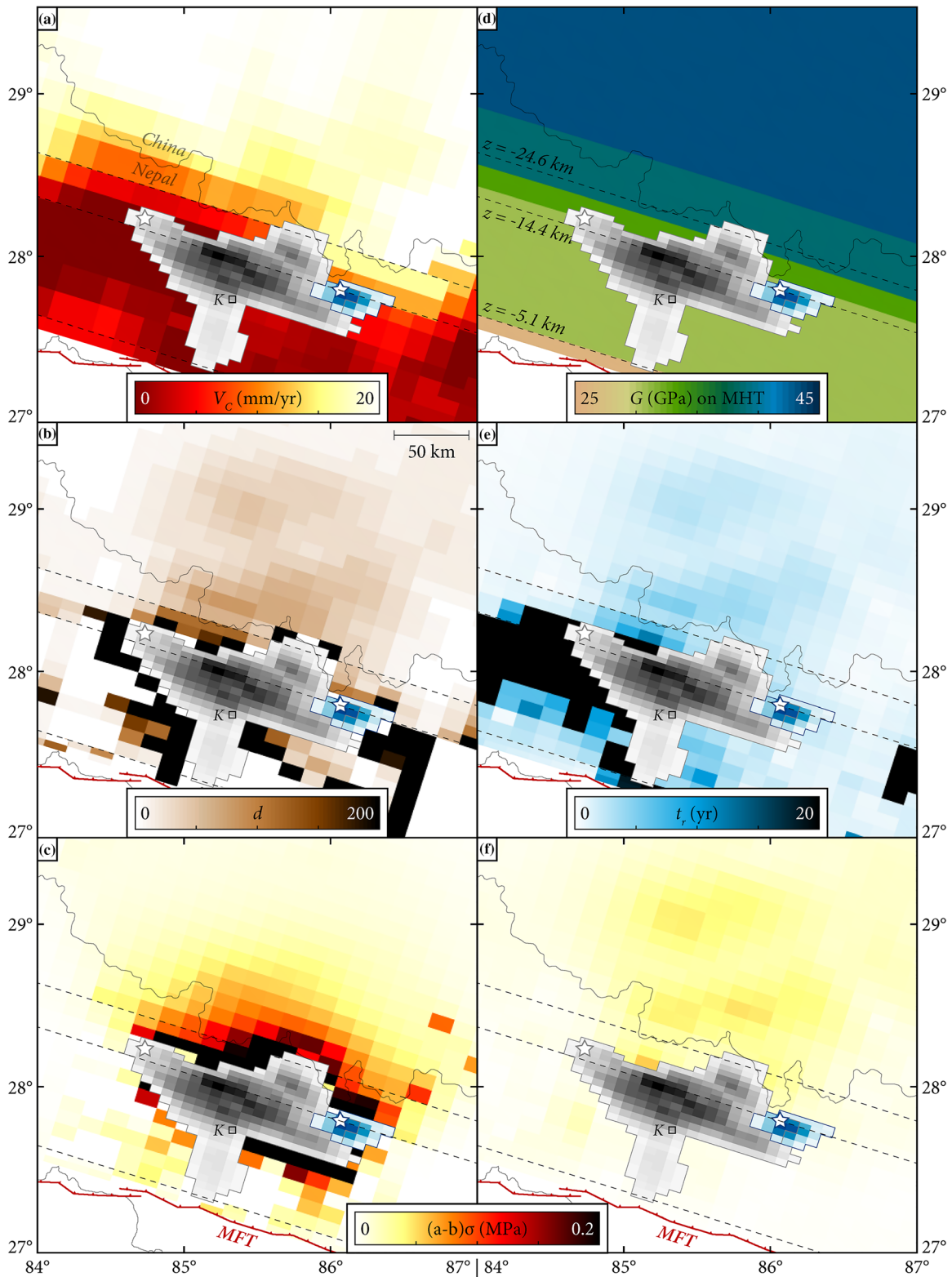


Figure 9. Estimates of $(a - b)\sigma$ (section 3) using the kinematic afterslip model (Figure 8). (a) Long-term sliding rate V_C derived from the interseismic coupling model (Figure 1a). (b) d , the factor by which each patch's slip velocity accelerated from the rate V_C after the mainshock. (c) $(a - b)\sigma$ as computed using d and the coseismic ΔCFF (Figure 2c) as per Equation 3. (d) The modeled shear modulus G on the MHT. (e) t_r , the estimated relaxation time of afterslip on each patch. (f) $(a - b)\sigma$ as calculated using these parameters (Equation 4). K = Kathmandu.

$$(a - b)\sigma = \frac{G}{W}V_C t_r, \quad (4)$$

where W is the characteristic size of the region of afterslip, for which we use 50 km based on the size of the major features in the kinematic model (Figure 8a), and G and V_C are the shear modulus and interseismic creep rate along each patch (Figures 9d and 9a).

The coseismic stress change decreases rapidly northward from the rupture (Figure 2), and the ΔCFF -based estimate of $(a - b)\sigma$ (Equation 3 and Figure 9c) shows that in order for this stress change to have induced a sufficient change in creep rates to ultimately yield the kinematic afterslip distribution in 1.12 yr, $(a - b)\sigma$ would need to decrease northward from ~ 0.5 MPa around the rupture to ≤ 0.05 MPa on the lower flat. Because this approach ignores the dynamic stress changes from afterslip itself, which could have enhanced its northward propagation, the estimated values of $(a - b)\sigma$ may be a lower bound. Nevertheless, the t_r -based estimate (Equation 4 and Figure 9f) agrees that $(a - b)\sigma$ would need to be ≤ 0.05 MPa on the lower flat in order for afterslip to have filled out such a large region while decaying in time like the first postseismic IC.

5. Dynamic Forward Afterslip Models

To test whether these kinematic models and interpretations are physically realistic, we use dynamic forward modeling to evaluate whether afterslip driven by coseismic and propagating stress changes could reproduce the postseismic displacements under plausible frictional conditions (e.g., Thomas et al., 2017). We use Relax (Barbot & Fialko, 2010a, 2010b), in which the constitutive law for stress-driven afterslip is a regularized form of the steady-state rate-strengthening friction law used above,

$$v = 2v_0 \sinh\left(\frac{\Delta\tau}{(a - b)\sigma}\right), \quad (5)$$

where v_0 and v are respectively the sliding velocities before and after a shear stress change $\Delta\tau$ is applied (Barbot et al., 2009). (The law used previously would give $v = v_0 \exp\left(\frac{\Delta\tau}{(a - b)\sigma}\right)$, which is equivalent to (4) except at small velocities, or $v = v_0 \exp\left(\frac{\Delta CFF}{(a - b)\sigma}\right)$, which is also essentially equivalent [Perfettini & Avouac, 2007], particularly as most of the coseismic stress changes are shear [Figure 2].) Due to the scant evidence of deformation updip of the rupture, we only simulate afterslip downdip of it. The models include the $M_w 7.3$ aftershock, and we allow afterslip on the possible stable-sliding region between the mainshock and aftershock (Figure 8a, dashed brown region; Supporting Information S2). We evaluate the model misfit using the time-integrated weighted root-mean-square error,

$$\frac{\chi^2}{N} = \frac{1}{N}(\mathbf{d}_{obs} - \mathbf{d}_{mod})^T \mathbf{C}_d^{-1} (\mathbf{d}_{obs} - \mathbf{d}_{mod}), \quad (6)$$

and the variance reduction,

$$VR = (\mathbf{d}_{obs} - \mathbf{d}_{mod})^T (\mathbf{d}_{obs} - \mathbf{d}_{mod}) (\mathbf{d}_{obs}^T \mathbf{d}_{obs})^{-1} \times 100(\%), \quad (7)$$

where \mathbf{d}_{obs} and \mathbf{d}_{mod} are respectively the concatenated vectors of observed and predicted three-component displacement time series from all stations, N is their length, and \mathbf{C}_d is a diagonal matrix of which the diagonal is the concatenated vector of data variance time series estimated from the vbICA applied to the postseismic timespan, doubled to account for uncertainties in the previous steps in the processing (1.12-yr values shown as ellipses in Figure 6a).

We first try a model with a uniform $(a - b)\sigma$ of 1 MPa, in the range inferred in other studies of afterslip (Barbot et al., 2009; Perfettini & Avouac, 2004, 2007; Thomas et al., 2017), and $v_0 = 20$ mm/yr, the approximate interseismic convergence rate (Stevens & Avouac, 2015). This model (Figure 10), which we refer to hereafter as the “basic forward afterslip model,” reproduces some of the south-southwest horizontal

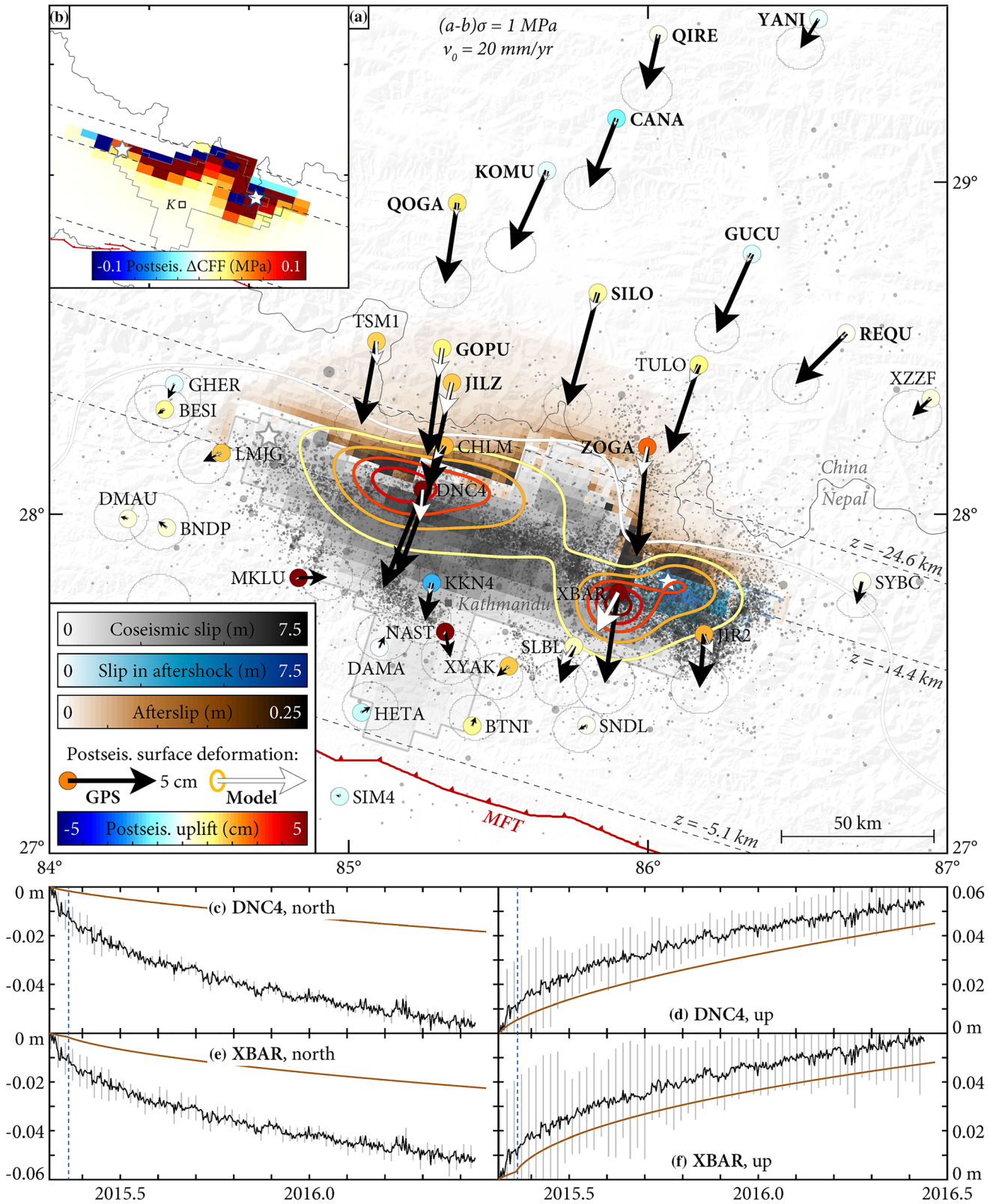


Figure 10. “Basic” forward afterslip model, in which $(a - b)\sigma = 1 \text{ MPa}$ and $v_0 = 20 \text{ mm/yr}$. (a) Cumulative 1.12-yr afterslip (brown) and surface displacements. Black/white arrows: Observed/predicted horizontal displacements. Colored circles/contours: Observed/predicted vertical displacements. Gray/blue stars and patches: Epicenters and slip in mainshock/ $M_w 7.3$ aftershock. (b) ΔCFE imparted by this afterslip to the coseismic rupture zone. (c–f) Observed (black/gray) and predicted (brown) displacement time series at DNC4 and XBAR. Blue dashed lines: Time of $M_w 7.3$ aftershock.

motion in the near field and most of the >5 cm of uplift at stations DNC4 and XBAR, with afterslip in between the mainshock and aftershock driving localized uplift at XBAR (Figures 10a and 10e). However, the model has two major shortcomings. First, the afterslip decays sharply northward from the downdip edge of the mainshock and produces very little displacement to the north in Tibet (Figure 10a), resulting in a poor overall fit to the GPS ($\chi^2/N = 4.40$, $VR = 33\%$; Table S1). Second, the model predicts that near-field stations would have a higher ratio of uplift to horizontal motion than observed in the data (Figures 10b and 10e). This ratio is also too high in models that use a planar MHT geometry. Because the ratios of near-field to far-field motion and near-field vertical to horizontal motion are both too high, increasing v_0 to fit the near-field horizontals, for example, causes models to overpredict the near-field verticals while still underpredicting the far-field horizontals (Figure S4). The same is seen in a model in which $v_0 = 20$ mm/yr and $(a - b)\sigma$ is lowered to 0.5 MPa (Figure S5).

A larger value of $(a - b)\sigma$ would in principle reduce the ratio of near-field to far-field afterslip because the function $\sinh\left(\frac{\Delta\tau}{(a - b)\sigma}\right)$ is strongly convex upward and increasing $(a - b)\sigma$ proportionally reduces it at large $\Delta\tau$ (near-field) compared to small $\Delta\tau$ (far-field). In particular, Jouanne et al. (2019) and Wang and Fialko (2018) respectively found that the best fitting $(a - b)\sigma$ values to characterize post-Gorkha afterslip were 6.5 and 22 MPa, and Tian et al. (2020) used $(a - b)\sigma = 5$ MPa. A potential drawback is that a larger $(a - b)\sigma$ requires invoking a larger reference creep rate v_0 : Jouanne et al. (2019), Tian et al. (2020), and Wang and Fialko (2018) respectively inferred $v_0 = 3.2 \times 10^{-7}$ m/s (10 m/yr), 0.2 m/yr, and 4.5×10^{-7} m/s (14 m/yr), much faster than the 20 mm/yr convergence rate. While acceleration by dynamic stresses could in theory account for some of this difference (Perfettini & Avouac, 2007), previous afterslip studies using the formalism of Equation 5 respectively inferred $v_0 \approx 20$ mm/yr for the Parkfield section of the San Andreas Fault (Barbot et al., 2009) and $v_0 \approx 5$ mm/yr for the Bam (Iran) region (Wimpenny et al., 2017), comparable to the interseismic deformation rate in both cases, and it is questionable whether the physics of afterslip on the MHT would allow v_0 to be the order of m/yr there. In fact, though, we find that models with a higher $(a - b)\sigma$ have shortcomings in fitting the data regardless of physical interpretation. A model with $(a - b)\sigma = 10$ MPa and $v_0 \sim 1$ m/yr overpredicts the near-field uplift (Figure S6a) while still underpredicting the displacements in Tibet, and it produces displacements that decay gradually in time as well as space, unlike the time evolution of the data (Figures S6b and S6c). Even an extreme model with $(a - b)\sigma = 100$ MPa and $v_0 \sim 10$ m/yr has the same limitations (Figure S7). This suggests that no afterslip model with uniform frictional properties can reproduce the northward reach of deformation.

We next hypothesize that v_0 might vary spatially. In particular, a northward increase in v_0 would also proportionally promote afterslip to the north (Equation 4). We try a model in which $(a - b)\sigma = 0.5$ MPa and v_0 increases northward following the interseismic creep rate (Figure 9a) (averaged laterally along the MHT). Compared to the model with $(a - b)\sigma = 0.5$ MPa and $v_0 = 20$ mm/yr (Figure S6), the lower v_0 values around the rupture in this model suppress slip and near-field deformation, and it does not overpredict the near-field vertical displacements (Figure S8a). However, it still underpredicts the horizontal displacements in Tibet (Figure S8a), inhibiting the total fit ($\chi^2/N = 3.70$, $VR = 41\%$).

This suggests that the postseismic displacement field could have been solely produced by afterslip if and only if $(a - b)\sigma$ decreases northward on the MHT, as inferred in the kinematic estimate using ΔCFF (Figure 8c).

(Mathematically, this would reduce the denominator of $\sinh\left(\frac{\Delta\tau}{(a - b)\sigma}\right)$ to the north, further proportionally promoting afterslip there.) We find that a model with uniform $v_0 = 35$ mm/yr and $(a - b)\sigma$ decreasing northward from 1 to 0.01 MPa can fit the horizontal displacement field (Figure 11a) and provide a better overall fit to the three components of the data ($\chi^2/N = 0.79$, $VR = 78\%$). We hereafter call this the “maximal forward afterslip model.” A model with $(a - b)\sigma$ decreasing downdip from 0.5 to 0.01 MPa and v_0 scaling with the laterally averaged interseismic creep rate, increasing northward to a maximum of 35 mm/yr (Figure S9), fits the data nearly equally well ($\chi^2/N = 0.79$, $VR = 76\%$).

However, neither of these models is physically convincing. As the Gorkha earthquake ruptured the north edge of the locked portion of the MHT (Figure 1a), $(a - b)\sigma$ should in principle increase northward from the rupture, not decrease northward, as it transitions from negative (rate-weakening) to positive (rate-strengthening) values. This is also predicted (and may be caused) by the northward increase in

temperature along the MHT (Figure 6a), which would be expected to enhance rate-strengthening behavior (Blanpied et al., 1991; den Hartog et al., 2012) rather than allowing $(a - b)\sigma$ to decrease to near zero. The temperature distribution casts further doubt on these broad afterslip models because midcrustal temperatures along the northward continuation of the MHT likely exceed 600°C (Herman et al., 2010; Wang et al., 2013) (Figures 6a and 6e), well above the typical 250–400°C temperature range for frictional afterslip (Blanpied et al., 1991; Thomas et al., 2017). At such temperatures ductile flow should be the dominant deformation mechanism.

6. Viscoelastic Relaxation in a Midcrustal Shear Zone

It therefore seems likely that the northward reach of the postseismic signal is at least partially the product of distributed viscoelastic relaxation. The MHT may extend north of the high Himalaya as a subhorizontal ductile shear zone (e.g., Bollinger et al., 2006; Cattin & Avouac, 2000), which could have viscoelastically relaxed the stress changes in the Gorkha earthquake, as hypothesized by Jouanne et al. (2019). We further test this hypothesis and assess the effective rheology of such a shear zone that is needed to explain the postseismic deformation revealed by the new data.

We note that our preferred kinematic and maximal forward afterslip models (Figures 8 and 11) already provide estimates of the displacement distributions on the extended MHT that are required to fit the postseismic data. Making use of this, we estimate the effective viscosities that would be implied by representing the MHT as a shear zone (Figures 12e and 12f) and assuming that these afterslip distributions represent the total 1.12-yr displacements between the top and bottom of the shear zone at each location. Dividing these distributions by the assumed shear-zone thickness and by 1.12 yr yields the distribution of strain rate across the shear zone averaged over that timespan. Then, dividing the shear stress change imparted by the mainshock and $M_w 7.3$ aftershock (Figure 2a) by this strain rate distribution yields the distribution of effective viscosity over the first 1.12 postseismic years. Assuming a 5-km-thick shear zone, the kinematic afterslip model (Figure 8) is equivalent to a distribution of effective viscosity that decreases northward from $\sim 10^{18}$ Pa·s around the coseismic rupture to $\sim 3 \cdot 10^{16}$ Pa·s ~ 100 km further north (Figure 12a). The maximal forward afterslip model (Figure 11) is equivalent to an effective viscosity distribution that decreases northward more gradually to $\sim 10^{17}$ Pa·s (Figure 12c). The effective viscosities would be four times higher if the shear zone were 20 km rather than 5 km thick: The kinematic and maximal forward afterslip models would respectively imply minimum viscosities of $\sim 10^{17}$ Pa·s (Figure 12b) and $\sim 3 \cdot 10^{17}$ Pa·s (Figure 12d). Although Jouanne et al. (2019) found that the best fitting width for a shear zone was ~ 3 – 4 km using post-Gorkha GPS data in Nepal, the estimated thermal structure (Figures 12e, 12g, and 12h) implies that a thermally activated shear zone would in fact likely increase northward in effective width, and so the 20-km-wide shear-zone models may be more realistic than the 5-km-wide models toward the north.

We can also estimate the effective viscosity from the preferred kinematic afterslip model by using the relaxation time t_r derived from the temporal decay of postseismic displacement (Figure 9e). Frictional afterslip and viscoelastic relaxation respectively predict that the time evolution of postseismic displacement should follow a logarithmic and an exponential function. We can determine the viscosity needed so that the two models would have the same first term in their Taylor expansions by multiplying t_r by the shear modulus G (Figure 9d). This yields estimated effective viscosities of $\sim 5 \cdot 10^{17}$ to $\sim 10^{18}$ Pa·s (Figure 12f), on the upper end of the values from the previous approach. One caveat is that this estimate relies on the temporal evolution of postseismic displacement, which was estimated from a single IC that is mostly influenced by near-field stations with larger postseismic signals. The previous shear-zone models (Figures 12a–12d), by contrast, are not sensitive to this aspect of the estimation.

7. Discussion and Conclusions

7.1. The Northward Reach of Postseismic Deformation and Its Implications

The new data assembled in this study reveal that postseismic deformation of the Gorkha earthquake extended >150 km north from the rupture into southern Tibet (Figures 3, 4, and 6a). This fills a gap between the near-field GPS and InSAR data used by most previous studies (Gualandi et al., 2017; Ingleby et al., 2020;

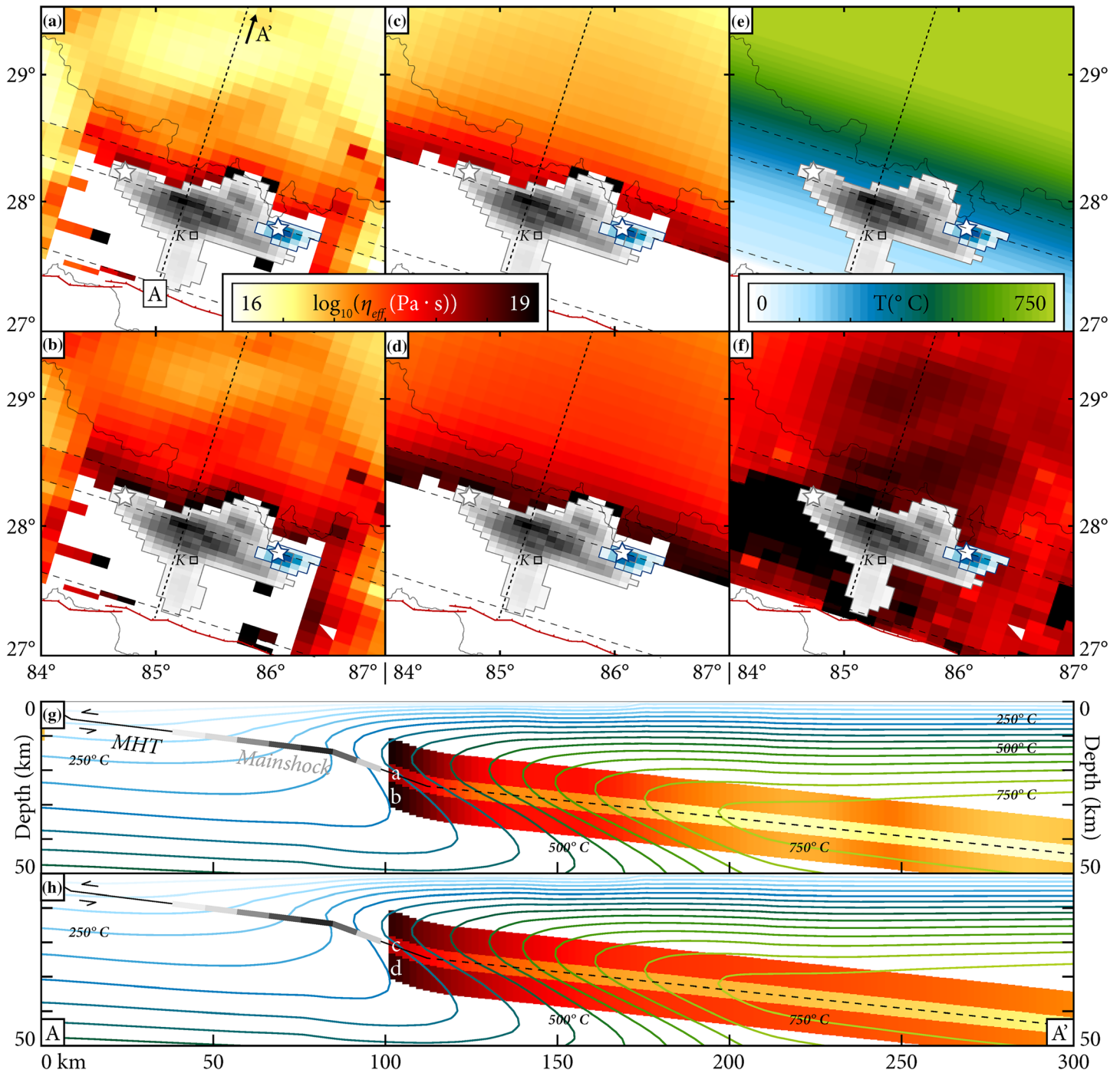


Figure 12. Estimated distributions of effective viscosity derived by equating the distributions of cumulative slip in the afterslip models to integrated shear across a viscous shear zone (section 6). (a, b) Effective viscosities derived from the distribution of slip in the preferred kinematic afterslip model (Figure 8), assuming a shear-zone width of 5 km (a) or 20 km (b). (c, d) Same as (c) except derived from the maximal forward afterslip model (Figure 11). (e) Estimated temperature on the MHT (Figure 6a). (f) Effective viscosities estimated using t_p , the estimated relaxation time of each patch in the kinematic afterslip model. (g) Cross sections of the estimated shear-zone viscosities in (a) and (b) (which are separate models) overlaid on the estimated temperature distribution. (h) The same as (e) except for the shear-zone models in (c) and (d).

Jouanne et al., 2019; Sreejith et al., 2016; Wang & Fialko, 2018) and the far-field GPS deformation included in the analyses of Jiang et al. (2018), Tian et al. (2020), and Zhao et al. (2017), allowing us to more clearly distinguish between possible causative processes. We infer, in agreement with Tian et al. (2020) and Zhao et al. (2017), that post-Gorkha deformation comprised a mix of afterslip and viscoelastic relaxation, with afterslip explaining features of the near-field deformation and viscoelastic relaxation contributing more in the far field.

Inverse and forward models (Figures 8 and 11) show that the broad pattern of post-Gorkha deformation could have been produced solely by afterslip on the MHT if and only if the afterslip extended >100 km north from the rupture. This would require the constitutive parameter $(a - b)\sigma$ to decrease northward to ≤ 0.05 MPa (Figures 9c, 9f, and 11). Models with larger values of $(a - b)\sigma$ on the lower flat of the MHT, or with $(a - b)\sigma$ assumed spatially uniform, do not reproduce the northward reach of postseismic displacements or their time evolution (Figures 10 and S4–S8). A value of ≤ 0.05 MPa for $(a - b)\sigma$ is well below the values of 0.5–1.5 MPa commonly inferred from afterslip observations (e.g., Barbot et al., 2009; Perfettini & Avouac, 2004, 2007; Thomas et al., 2017). Such low $(a - b)\sigma$ values would imply an extreme sensitivity of sliding rate to stress change (i.e., that slip is barely aseismic), which seems unlikely as the interseismic coupling distribution (Figure 1a) and the high midcrustal temperatures to the north (Figures 6a and 6b) imply that the northward continuation of the MHT should be stably deforming (Figure 9a). Gualandi et al. (2014) estimated a comparably low value of $(a - b)\sigma$ for afterslip of the 2009 L'Aquila earthquake, but that afterslip occurred in a transition from rate-weakening to rate-strengthening behavior, whereas here it would presumably be tens of km north of that transition on the MHT (Figure 1a). More fundamentally, temperatures likely exceed 600°C on the lower flat beneath Tibet, well above the 250–400°C range optimal for afterslip to occur at all (Blanpied et al., 1991; Perfettini & Avouac, 2004).

This *reductio ad absurdum* suggests that distributed viscoelastic relaxation is a more plausible mechanism to explain the northward reach of surface displacements (section 6). This is consistent with findings from studies of postseismic deformation following many subduction zone earthquakes (e.g., Freed et al., 2017; Klein et al., 2016; Qiu et al., 2018; Suito & Freymueller, 2009; Weiss et al., 2019) and large earthquakes in most tectonic environments (Freed et al., 2006; Gualandi et al., 2020; Wright et al., 2013). In the post-Gorkha case, this viscoelastic relaxation could occur within a shear zone that accommodates India-Tibet convergence as the northward continuation of the brittle MHT (e.g., Cattin & Avouac, 2000; Jouanne et al., 2019). We use the distributions of cumulative slip in our preferred kinematic and maximal forward afterslip models as estimates of the postseismic displacement that would be required across this shear zone and use this to estimate its effective postseismic viscosity. These models imply that the effective viscosity would decrease northward from 10^{18} – 10^{19} Pa·s around the rupture to $\sim 3 \cdot 10^{16}$ – 10^{18} Pa·s ~ 150 km north, depending on the effective width of the shear zone and the estimation method (Figure 12).

Among previous studies of post-Gorkha deformation, Jouanne et al. (2019) also modeled a shear zone extending northward from the MHT and inferred an effective postseismic viscosity of 10^{16} Pa·s for the shear zone using GPS data in Nepal (acknowledging that the limitations of their data set made the contribution of viscoelastic relaxation difficult to distinguish). We note that Jouanne et al. inferred an optimal shear-zone width of 3–4 km, which would require a higher strain rate across the shear zone and thus a lower effective viscosity. Wang and Fialko (2018), Tian et al. (2020), and Zhao et al. (2017) modeled viscoelastic relaxation in a ductile layer below the northward extension of the MHT rather than continuing northward from it; of these, Wang and Fialko (2018) and Zhao et al. (2017) respectively inferred transient viscosities of $\sim 8 \cdot 10^{18}$ and $\gg 10^{18}$ Pa·s for this layer, and Tian et al. (2020) (who used longer time series) inferred a transient viscosity of $5 \cdot 10^{17}$ Pa·s. Among other studies on the Tibetan Plateau, Huang et al. (2014) and Ryder et al. (2011) inferred transient viscosities of $9 \cdot 10^{17}$ and $4.4 \cdot 10^{17}$ Pa·s from postseismic deformation following the 2001 Kokoxili and 2008 Wenchuan earthquakes, respectively. In comparing our viscosity estimates with these, four caveats are worth noting. First, our estimates ignore the possible contribution of afterslip, which may in particular have occurred around the downdip edge of the rupture (see below). Second, they ignore the dynamic propagating stress changes from viscoelastic relaxation, as well as those induced by any afterslip. These two caveats imply that the true effective postseismic viscosities may be somewhat higher than estimated here. Third, we characterize the postseismic deformation using a single IC, which is likely mostly influenced by near-field stations with large signals that may have been partially driven by afterslip. This

would in particular bias the viscosity estimate using the relaxation time t_r of postseismic displacements (Figure 12f). Finally, the time evolution of the first postseismic IC (Figure 5d) implies that strain rates were highest just after the earthquake, or equivalently that the effective viscosity was lowest then. Our shear-zone estimates (Figures 12a–12d) are average 1.12-yr values, and so they would not capture this time dependence. Despite these caveats, our estimates fall in the middle of the range of values inferred from previous studies of postseismic deformation in this region; in particular, their agreement with the post-Gorkha estimate of Tian et al. (2020) is encouraging. The deformation of early Holocene paleolake high-stand shorelines in southern Tibet implies that the long-term viscosity of the middle crust of Tibet is $>10^{18}$ Pa·s (England et al., 2013; Henriquet et al., 2019), and so the estimates derived here likely represent a transient viscosity that may be less prevalent over such timescales.

7.2. Afterslip Fringing the Coseismic Rupture

The deformation closer to the Gorkha rupture, meanwhile, can more plausibly be explained as indeed resulting from afterslip itself. Most previous studies of post-Gorkha deformation kinematically inferred the presence of afterslip fringing the downdip edge of the rupture and on the possible stable-sliding region between the mainshock and aftershock (Gualandi et al., 2017; Jiang et al., 2018; Sreejith et al., 2016; Tian et al., 2020; Wang & Fialko, 2018; Zhao et al., 2017). Our dynamic forward models reproduce afterslip directly up to the lower edge of the rupture and in between the mainshock and aftershock (Figures 10 and 11), decaying sharply and evenly northward in amplitude as expected of a stress-change-driven process. Like Ingleby et al. (2020), this physical realism allows us to use these models to robustly qualify what role near-field afterslip could have played in the postseismic displacement field. This has the secondary advantage of ensuring that the aforementioned findings about far-field deformation are minimally biased by limitations of the near-field modeling, but it also yields several findings on its own. These findings are that near-field afterslip can explain the localized uplift seen around stations DNC4 and XBAR (Figure 10) and some of the south-southwest horizontal motion but predicts ratios of near-field to far-field motion and near-field vertical to horizontal motion that are both higher than the ratios observed. This places an upper bound on the likely contribution of afterslip to post-Gorkha deformation.

Two models that lie within this bound, by reproducing the localized near-field uplift without overpredicting any aspect of the observations, are the basic forward afterslip model (Figure 10), in which $(a - b)\sigma = 1$ MPa and $v_0 = 20$ mm/yr, and the model in which $(a - b)\sigma = 0.5$ MPa and v_0 increases northward from near zero to 20 mm/yr (Figure S8a) following the interseismic creep rates (Figure 9a). These models may comprise reasonable estimates of the true contribution of afterslip and would imply a local value of $(a - b)\sigma \approx 0.5$ –1 MPa in the near-field region, consistent with studies of afterslip following other earthquakes (e.g., Barbot et al., 2009; Perfettini & Avouac, 2004, 2007; Thomas et al., 2017). In their analysis of post-Gorkha deformation (which they inferred was predominantly afterslip), Ingleby et al. (2020) estimated a value of $a = 0.8$ –1.6 for the MHT just north of the rupture (using $a\sigma$ rather than $(a - b)\sigma$). With their assumed value of $\sigma = 350$ MPa, this would imply $(a - b)\sigma \approx 0.3$ –0.6 MPa. Despite differences in data and modeling approaches, this is comparable to our inferred value of $(a - b)\sigma \approx 0.5$ –1 MPa. It makes sense that Ingleby et al.'s (2020) estimate would be somewhat lower as their model is fit to all available post-Gorkha data and may include some deformation to the north that we characterize as viscoelastic. This is effectively the converse of the caveat that our viscoelastic estimates above may include some afterslip-related deformation; it would also apply to our maximal forward afterslip model (Figure 11). At any rate, it seems plausible that postseismic deformation near the rupture was driven by afterslip, perhaps similar to the parametrization of the basic forward model, while deformation further northward was driven by viscoelastic relaxation in a shear zone or ductile substrate. This would reflect a northward transition from seismic slip to aseismic creep to ductile flow (e.g., Perfettini & Avouac, 2004).

7.3. The Magnitude and Stress Implications of Post-Gorkha Deformation

Using our kinematic models (Supporting Information S3), we estimate that in the first 1.12 yr after the Gorkha earthquake, postseismic deformation beneath Nepal and Tibet released a total elastic strain equivalent to a moment between $[1.21 \pm 0.15] \times 10^{20}$ Nm and $[2.37 \pm 0.13] \times 10^{20}$ Nm, equivalent to a M_w 7.3–7.5 earthquake. For comparison, Zhao et al. (2017) and Jiang et al. (2018) inferred a moment release of 10^{20} and 1.2×10^{20} Nm over the first 1.0 and 1.6 postseismic years, respectively, at the lower end of this range. This

dwarfs the estimated 2.98×10^{19} Nm ($M_w \sim 6.9$) total moment released by aftershocks (Figure 8a) over this period (Supporting Information S3), making it clear that postseismic deformation was >75% aseismic. Finally, using our maximal forward afterslip model, we estimate that this postseismic deformation (by itself) re-increased the Coulomb stress by ≥ 0.05 MPa (Figure 11b) over $\sim 40\%$ of the Gorkha earthquake rupture zone (defined here as the area of ≥ 0.25 m slip in the Elliott et al., 2016, model). Even if afterslip fringing the rupture were the only postseismic deformation, as in the basic forward afterslip model, this number would still be 32% (Figure 10b). For comparison, the stress drop in the Gorkha earthquake is estimated at ~ 5 MPa on average (Galetzka et al., 2015), and the rate of interseismic stress loading on the Gorkha rupture zone is estimated at $\sim 1\text{--}5$ kPa/yr (Cattin & Avouac, 2000). Postseismic reloading in the first 1.12 yr following the Gorkha earthquake therefore amounted to the equivalent of one to several decades of interseismic loading and was superimposed on that loading. This would compound the seismic hazard in the Nepal Himalaya, which remains high particularly along the locked updip section of the MHT and west and east of the Gorkha earthquake.

Data Availability Statement

The data are published in the repository <http://tectonics.caltech.edu/resources/gorkha.html> as follows:

1. ITRF2008_midday_ODRENGL.zip are the time series at 171 stations in ITRF2008 (light gray in Figures 3 and 4).
2. Indiafixed_midday_detrended_deseasonal_rmoffsets_rmaftershock_errpropagation_ODRENGL.zip are the post-Gorkha portions of the time series at 94 stations with trends, seasonal signals, and post-Gorkha offsets removed (blue in Figures 3 and 4).
3. Liuetal_2020_postseismicIC1.zip are the time series of the first postseismic Independent Component at the 67 stations that have data over $\geq 20\%$ of the postseismic period (black in Figures 3 and 4).
4. Liu_etal_ITRF2008ts_UNRcomparison.zip contains plots comparing our time series in ITRF2008 (Figures 3 and 4, light gray) with those from the Nevada Geodetic Laboratory (NGL).
5. vel_interp_ODRENGL.txt gives the estimated India-relative linear velocities at all stations (main text section 2; Figures 3 and 4, orange; Figures 5 and 7, red arrows).
6. vel_Indiafixed_literatureunified.txt gives India-relative velocities from literature (section 2; Figures 5 and 7, gray arrows).
7. offsets_estimated_Indiafixed_ODRENGL.txt specifies offsets estimated and removed from the India-relative time series.

The 13 new stations are bolded in Figures 1, 6, and 8.

Acknowledgments

We are indebted to Sylvain Barbot and an anonymous reviewer for providing suggestions and feedback that greatly improved the manuscript. We thank Lisa Christiansen and Naveed Near-Ansari for technical assistance. J. L.-Z. was supported by the National Natural Science Foundation of China (NSFC) (41761144065 and U1839203) and Basic Research Fund for Central Scientific Institutes (IGCEA 1206 and 1812). J.-P. A. was supported by National Science Foundation (NSF) Award EAR-1821853.

References

- Ader, T., Avouac, J. P., Liu-Zeng, J., Lyon-Caen, H., Bollinger, L., Galetzka, J., et al. (2012). Convergence rate across the Nepal Himalaya and interseismic coupling on the Main Himalayan Thrust: Implications for seismic hazard. *Journal of Geophysical Research*, *117*, B04403. <https://doi.org/10.1029/2011JB009071>
- Altamimi, Z., Collilieux, X., & Métivier, L. (2011). ITRF2008: An improved solution of the international terrestrial reference frame. *Journal of Geodesy*, *85*(8), 457–473. <https://doi.org/10.1007/s00190-011-0444-4>
- Avouac, J.-P., Meng, L., Wei, S., Wang, T., & Ampuero, J.-P. (2015). Lower edge of locked Main Himalayan Thrust unzipped by the 2015 Gorkha earthquake. *Nature Geoscience*, *8*(9), 708–711. <https://doi.org/10.1038/ngeo2518>
- Baillard, C., Lyon-Caen, H., Bollinger, L., Rietbrock, A., Letort, J., & Adhikari, L. B. (2017). Automatic analysis of the Gorkha earthquake aftershock sequence: Evidences of structural segmented seismicity. *Geophysical Journal International*, *209*(2), 1111–1125. <https://doi.org/10.1093/gji/ggx081>
- Banerjee, P., & Bürgmann, R. (2002). Convergence across the northwest Himalaya from GPS measurements. *Geophysical Research Letters*, *29*(13), 1652. <https://doi.org/10.1029/2002GL015184>
- Barbot, S., & Fialko, Y. (2010a). Fourier-domain Green's function for an elastic semi-infinite solid under gravity, with applications to earthquake and volcano deformation. *Geophysical Journal International*, *182*(2), 568–582. <https://doi.org/10.1111/j.1365-246X.2010.04655.x>
- Barbot, S., & Fialko, Y. (2010b). A unified continuum representation of post-seismic relaxation mechanisms: Semi-analytic models of afterslip, poroelastic rebound and viscoelastic flow. *Geophysical Journal International*, *182*(3), 1124–1140. <https://doi.org/10.1111/j.1365-246X.2010.04678.x>
- Barbot, S., Fialko, Y., & Bock, Y. (2009). Postseismic deformation due to the M_w 6.0 2004 Parkfield earthquake: Stress-driven creep on a fault with spatially variable rate-and-state friction parameters. *Journal of Geophysical Research*, *114*, B07405. <https://doi.org/10.1029/2008JB005748>
- Bettinelli, P., Avouac, J. P., Flouzat, M., Bollinger, L., Ramillien, G., Rajaure, S., & Sapkota, S. (2008). Seasonal variations of seismicity and geodetic strain in the Himalaya induced by surface hydrology. *Earth and Planetary Science Letters*, *266*(3–4), 332–344. <https://doi.org/10.1016/j.epsl.2007.11.021>

- Bettinelli, P., Avouac, J.-P., Flouzat, M., Jouanne, F., Bollinger, L., Willis, P., & Chitrakar, G. R. (2006). Plate motion of India and interseismic strain in the Nepal Himalaya from GPS and DORIS measurements. *Journal of Geodesy*, *80*(8–11), 567–589. <https://doi.org/10.1007/s00190-006-0030-3>
- Bevis, M., & Brown, A. (2014). Trajectory models and reference frames for crustal motion geodesy. *Journal of Geodesy*, *88*(3), 283–311. <https://doi.org/10.1007/s00190-013-0685-5>
- Blanpied, M., Lockner, D., & Byerlee, J. (1991). Fault stability inferred from granite sliding experiments at hydrothermal condition. *Geophysical Research Letters*, *18*(4), 609–612. <https://doi.org/10.1029/91GL00469>
- Blewitt, G., Hammond, W. C., & Kreemer, C. (2018). Harnessing the GPS data explosion for interdisciplinary science, *Eos*, *99*, 1–2. <https://doi.org/10.1029/2018EO104623>
- Bollinger, L., Henry, P., & Avouac, J.-P. (2006). Mountain building in the Nepal Himalaya: Thermal and kinematic model. *Earth and Planetary Science Letters*, *244*(1–2), 58–71. <https://doi.org/10.1016/j.epsl.2006.01.045>
- Calais, E., Dong, L., Wang, M., Shen, Z., & Vergnolle, M. (2006). Continental deformation in Asia from a combined GPS solution. *Geophysical Research Letters*, *33*, L24319. <https://doi.org/10.1029/2006GL028433>
- Cattin, R., & Avouac, J. P. (2000). Modeling mountain building and the seismic cycle in the Himalaya of Nepal. *Journal of Geophysical Research*, *105*(B6), 13,389–13,407. <https://doi.org/10.1029/2000JB900032>
- Chlieh, M., Avouac, J. P., Sieh, K., Natawidjaja, D. H., & Galetzka, J. (2008). Heterogeneous coupling of the Sumatran megathrust constrained by geodetic and paleogeodetic measurements. *Journal of Geophysical Research: Solid Earth*, *113*, B05305. <https://doi.org/10.1029/2007JB004981>
- Chopra, S., Sharma, J., Sutar, A., & Bansal, B. K. (2014). Estimation of source parameters of Mw 6.9 Sikkim earthquake and modeling of ground motions to determine causative fault. *Pure and Applied Geophysics*, *171*, 1311–1328. <https://doi.org/10.1007/s00024-013-0722-6>
- Choudrey, R. A., & Roberts, S. J. (2003). Variational mixture of Bayesian independent component analyzers. *Neural Computation*, *15*(1), 213–252. <https://doi.org/10.1162/089976603321043766>
- den Hartog, S. A. M., Peach, C. J., de Winter, D. A. M., Spiers, C. J., & Shimamoto, T. (2012). Frictional properties of megathrust fault gouges at low sliding velocities: New data on effects of normal stress and temperature. *Journal of Structural Geology*, *38*, 156–171. <https://doi.org/10.1016/j.jsg.2011.12.001>
- Duong, C. C., Yun, H.-S., & Cho, J.-M. (2006). GPS measurements of horizontal deformation across the Lai Chau-Dien Bien (Dien Bien Phu) fault, in Northwest of Vietnam, 2002–2004. *Earth, Planets and Space*, *58*(5), 523–528. <https://doi.org/10.1186/BF03351949>
- Elliott, J. R., Jolivet, R., Gonzalez, P. J., Avouac, J. P., Hollingsworth, J., Searle, M. P., & Stevens, V. L. (2016). Himalayan megathrust geometry and relation to topography revealed by the Gorkha earthquake. *Nature Geoscience*, *9*(2), 174–180. <https://doi.org/10.1038/ngeo2623>
- England, P. C., Walker, R. T., Fu, B. H., & Floyd, M. A. (2013). A bound on the viscosity of the Tibetan crust from the horizontality of palaeolake shorelines. *Earth and Planetary Science Letters*, *375*, 44–56. <https://doi.org/10.1016/j.epsl.2013.05.001>
- Freed, A. M., Bürgmann, R., Calais, E., & Freymueller, J. (2006). Stress-dependent power-law flow in the upper mantle following the 2002 Denali, Alaska, earthquake. *Earth and Planetary Science Letters*, *252*(3–4), 481–489. <https://doi.org/10.1016/j.epsl.2006.10.011>
- Freed, A. M., Hashima, A., Becker, T. W., Okaya, D. A., Sato, H., & Hatanaka, Y. (2017). Resolving depth-dependent subduction zone viscosity and afterslip from postseismic displacements following the 2011 Tohoku-oki, Japan earthquake. *Earth and Planetary Science Letters*, *459*, 279–290. <https://doi.org/10.1016/j.epsl.2016.11.040>
- Gahalaut, V. K., Kundu, B., Laishram, S. S., Catherine, J., Kumar, A., Singh, M. D., et al. (2013). Aseismic plate boundary in the Indo-Burmese wedge, northwest Sunda Arc. *Geology*, *41*(2), 235–238. <https://doi.org/10.1130/G33771.1>
- Galetzka, J., Melgar, D., Genrich, J. F., Geng, J., Owen, S., Lindsey, E. O., et al. (2015). Slip pulse and resonance of the Kathmandu basin during the 2015 Gorkha earthquake, Nepal. *Science*, *349*(6252), 1091–1095. <https://doi.org/10.1126/science.aac6383>
- Gan, W., Zhang, P., Shen, Z. K., Niu, Z., Wang, M., Wan, Y., et al. (2007). Present-day crustal motion within the Tibetan Plateau inferred from GPS measurements. *Journal of Geophysical Research*, *112*, B08416. <https://doi.org/10.1029/2005JB004120>
- Gualandi, A., Avouac, J. P., Galetzka, J., Genrich, J. F., Blewitt, G., Adhikari, L. B., et al. (2017). Pre- and post-seismic deformation related to the 2015, M_w 7.8 Gorkha earthquake, Nepal. *Tectonophysics*, *714*, 90–106.
- Gualandi, A., Liu, Z., & Rollins, C. (2020). Post-large earthquake seismic activities mediated by aseismic deformation processes. *Earth and Planetary Science Letters*, *530*, 115870. <https://doi.org/10.1016/j.epsl.2019.115870>
- Gualandi, A., Serpelloni, E., & Belardinelli, M. E. (2014). Space-time evolution of crustal deformation related to the M_w 6.3, 2009 L'Aquila earthquake (central Italy) from principal component analysis inversion of GPS position time-series. *Geophysical Journal International*, *197*(1), 174–191. <https://doi.org/10.1093/gji/ggt522>
- Gualandi, A., Serpelloni, E., & Belardinelli, M. E. (2016). Blind source separation problem in GPS time series. *Journal of Geodesy*, *90*(4), 323–341. <https://doi.org/10.1007/s00190-015-0875-4>
- Gupta, T. D., Riguzzi, F., Dasgupta, S., Mukhopadhyay, B., Roy, S., & Sharma, S. (2015). Kinematics and strain rates of the Eastern Himalayan Syntaxis from new GPS campaigns in Northeast India. *Tectonophysics*, *655*, 15–26. <https://doi.org/10.1016/j.tecto.2015.04.017>
- He, J., Lu, S., & Wang, W. (2013). Three-dimensional mechanical modeling of the GPS velocity field around the northeastern Tibetan plateau and surrounding regions. *Tectonophysics*, *584*, 257–266. <https://doi.org/10.1016/j.tecto.2012.03.025>
- Henriquet, M., Avouac, J. P., & Bills, B. G. (2019). Crustal rheology of southern Tibet constrained from lake-induced viscoelastic deformation. *Earth and Planetary Science Letters*, *506*, 308–322. <https://doi.org/10.1016/j.epsl.2018.11.014>
- Henry, P., Le Pichon, X., & Goffé, B. (1997). Kinematic, thermal and petrological model of the Himalayas: Constraints related to metamorphism within the underthrust Indian crust and topographic elevation. *Tectonophysics*, *273*(1–2), 31–56. [https://doi.org/10.1016/S0040-1951\(96\)00287-9](https://doi.org/10.1016/S0040-1951(96)00287-9)
- Herman, F., Copeland, P., Avouac, J. P., Bollinger, L., Mahéo, G., Le Fort, P., et al. (2010). Exhumation, crustal deformation, and thermal structure of the Nepal Himalaya derived from the inversion of thermochronological and thermobarometric data and modeling of the topography. *Journal of Geophysical Research*, *115*, B06407. <https://doi.org/10.1029/2008JB006126>
- Herring, T. A., King, R. W., Floyd, M. A., & McClusky, S. C. (2015). *Introduction to GAMIT/GLOBK, Release 10.6*. Cambridge: Massachusetts Institute of Technology.
- Hsu, Y.-J., Yu, S.-B., Simons, M., Kuo, L.-C., & Chen, H.-Y. (2009). Interseismic crustal deformation in the Taiwan plate boundary zone revealed by GPS observations, seismicity, and earthquake focal mechanisms. *Tectonophysics*, *479*(1–2), 4–18. <https://doi.org/10.1016/j.tecto.2008.11.016>
- Huang, M.-H., Bürgmann, R., & Freed, A. M. (2014). Probing the lithospheric rheology across the eastern margin of the Tibetan Plateau. *Earth and Planetary Science Letters*, *396*, 88–96. <https://doi.org/10.1016/j.epsl.2014.04.003>

- Ingleby, T., Wright, T. J., Hooper, A., Craig, T. J., & Elliott, J. R. (2020). Constraints on the rheology and frictional properties of the Main Himalayan Thrust using coseismic, postseismic, and interseismic deformation in Nepal. *Journal of Geophysical Research: Solid Earth*, *125*, e2019JB019201. <https://doi.org/10.1029/2019JB019201>
- Ischuk, A., Bendick, R., Rybin, A., Molnar, P., Khan, S. F., Kuzikov, S., et al. (2013). Kinematics of the Pamir and Hindu Kush regions from GPS geodesy. *Journal of Geophysical Research: Solid Earth*, *118*, 2408–2416. <https://doi.org/10.1002/jgrb.50185>
- Jade, S. (2004). Estimates of plate velocity and crustal deformation in the Indian subcontinent using GPS geodesy. *Current Science*, *86*(10), 1443–1448.
- Jade, S., Mukul, M., Bhattacharyya, A. K., Vijayan, M., Jaganathan, S., Kumar, A., et al. (2007). Estimates of interseismic deformation in Northeast India from GPS measurements. *Earth and Planetary Science Letters*, *263*(3–4), 221–234. <https://doi.org/10.1016/j.epsl.2007.08.031>
- Jade, S., Mukul, M., Gaur, V., Kumar, K., Shringeshwar, T., Satyal, G., et al. (2014). Contemporary deformation in the Kashmir–Himachal, Garhwal and Kumaon Himalaya: Significant insights from 1995–2008 GPS time series. *Journal of Geodesy*, *88*(6), 539–557. <https://doi.org/10.1007/s00190-014-0702-3>
- Jade, S., Rao, H. R., Vijayan, M., Gaur, V., Bhatt, B., Kumar, K., et al. (2011). GPS-derived deformation rates in northwestern Himalaya and Ladakh. *International Journal of Earth Sciences*, *100*(6), 1293–1301. <https://doi.org/10.1007/s00531-010-0532-3>
- Jiang, Z. S., Yuan, L. G., Huang, D. F., Yang, Z. R., & Hassan, A. (2018). Postseismic deformation associated with the 2015 Mw 7.8 Gorkha earthquake, Nepal: Investigating ongoing afterslip and constraining crustal rheology. *Journal of Asian Earth Sciences*, *156*, 1–10. <https://doi.org/10.1016/j.jseae.2017.12.039>
- Jouanne, F., Awan, A., Pêcher, A., Kausar, A., Mugnier, J., Khan, I., et al. (2014). Present-day deformation of northern Pakistan from Salt Ranges to Karakorum Ranges. *Journal of Geophysical Research: Solid Earth*, *119*, 2487–2503. <https://doi.org/10.1002/2013JB010776>
- Jouanne, F., Gajurel, A., Mugnier, J. L., Bollinger, L., Adhikari, L. B., Koirala, B., et al. (2019). Postseismic deformation following the April 25, 2015 Gorkha earthquake (Nepal): Afterslip versus viscous relaxation. *Journal of Asian Earth Sciences*, *176*, 105–119. <https://doi.org/10.1016/j.jseae.2019.02.009>
- Jouanne, F., Mugnier, J. L., Sapkota, S. N., Bascou, P., & Pecher, A. (2017). Estimation of coupling along the Main Himalayan Thrust in the central Himalaya. *Journal of Asian Earth Sciences*, *133*, 62–71. <https://doi.org/10.1016/j.jseae.2016.05.028>
- Klein, E., Fleitout, L., Vigny, C., & Garaud, J. (2016). Afterslip and viscoelastic relaxation model inferred from the large-scale post-seismic deformation following the 2010 M_w 8.8 Maule earthquake (Chile). *Geophysical Journal International*, *205*(3), 1455–1472. <https://doi.org/10.1093/gji/ggw086>
- Kositsky, A. P., & Avouac, J. P. (2010). Inverting geodetic time series with a principal component analysis-based inversion method. *Journal of Geophysical Research*, *115*, B03401. <https://doi.org/10.1029/2009JB006535>
- Kundu, B., Yadav, R. K., Bali, B. S., Chowdhury, S., & Gahalaut, V. (2014). Oblique convergence and slip partitioning in the NW Himalaya: Implications from GPS measurements. *Tectonics*, *33*, 2013–2024. <https://doi.org/10.1002/2014TC003633>
- Larochelle, S., Gualandi, A., Chanard, K., & Avouac, J. P. (2018). Identification and extraction of seasonal geodetic signals due to surface load variations. *Journal of Geophysical Research: Solid Earth*, *123*, 11,031–11,047. <https://doi.org/10.1029/2018JB016607>
- Liang, S., Gan, W., Shen, C., Xiao, G., Liu, J., Chen, W., et al. (2013). Three-dimensional velocity field of present-day crustal motion of the Tibetan Plateau derived from GPS measurements. *Journal of Geophysical Research: Solid Earth*, *118*, 5722–5732. <https://doi.org/10.1002/2013JB010503>
- Lindsey, E. O., Natsuaki, R., Xu, X., Shimada, M., Hashimoto, M., Melgar, D., & Sandwell, D. T. (2015). Line-of-sight displacement from ALOS-2 interferometry: M_w 7.8 Gorkha Earthquake and M_w 7.3 aftershock. *Geophysical Research Letters*, *42*, 6655–6661. <https://doi.org/10.1002/2015GL065385>
- Mahesh, P., Catherine, J., Gahalaut, V., Kundu, B., Ambikapathy, A., Bansal, A., et al. (2012). Rigid Indian plate: Constraints from GPS measurements. *Gondwana Research*, *22*(3–4), 1068–1072. <https://doi.org/10.1016/j.gr.2012.01.011>
- Marechal, A., Mazzotti, S., Cattin, R., Cazes, G., Vernant, P., Drukpa, D., et al. (2016). Evidence of interseismic coupling variations along the Bhutan Himalayan arc from new GPS data. *Geophysical Research Letters*, *43*, 12,399–12,406. <https://doi.org/10.1002/2016GL071163>
- Maurin, T., Masson, F., Rangin, C., Min, U. T., & Collard, P. (2010). First global positioning system results in northern Myanmar: Constant and localized slip rate along the Sagaing fault. *Geology*, *38*(7), 591–594. <https://doi.org/10.1130/G30872.1>
- Mohadjer, S., Bendick, R., Ischuk, A., Kuzikov, S., Kostuk, A., Saydullaev, U., et al. (2010). Partitioning of India-Eurasia convergence in the Pamir-Hindu Kush from GPS measurements. *Geophysical Research Letters*, *37*, L04305. <https://doi.org/10.1029/2009GL041737>
- Mukul, M., Jade, S., Bhattacharyya, A. K., & Bhusan, K. (2010). Crustal shortening in convergent orogens: Insights from global positioning system (GPS) measurements in northeast India. *Journal of the Geological Society of India*, *75*(1), 302–312. <https://doi.org/10.1007/s12594-010-0017-9>
- Perfettini, H., & Avouac, J. P. (2004). Postseismic relaxation driven by brittle creep: A possible mechanism to reconcile geodetic measurements and the decay rate of aftershocks, application to the Chi-Chi earthquake, Taiwan. *Journal of Geophysical Research*, *109*, B02304. <https://doi.org/10.1029/2003JB002488>
- Perfettini, H., & Avouac, J. P. (2007). Modeling afterslip and aftershocks following the 1992 Landers earthquake. *Journal of Geophysical Research*, *112*, B07409. <https://doi.org/10.1029/2006JB004399>
- Ponraj, M., Miura, S., Reddy, C., Amirtharaj, S., & Mahajan, S. (2011). Slip distribution beneath the Central and Western Himalaya inferred from GPS observations. *Geophysical Journal International*, *185*(2), 724–736. <https://doi.org/10.1111/j.1365-246X.2011.04958.x>
- Qiu, Q., Moore, J. D., Barbot, S., Feng, L., & Hill, E. M. (2018). Transient rheology of the Sumatran mantle wedge revealed by a decade of great earthquakes. *Nature Communications*, *9*, 995. <https://doi.org/10.1038/s41467-018-03298-6>
- Radiguet, M., Cotton, F., Vergnolle, M., Campillo, M., Valette, B., Kostoglodov, V., & Cotte, N. (2011). Spatial and temporal evolution of a long term slow slip event: The 2006 Guerrero Slow Slip Event. *Geophysical Journal International*, *184*(2), 816–828. <https://doi.org/10.1111/j.1365-246X.2010.04866.x>
- Ryder, I., Bürgmann, R., & Pollitz, F. (2011). Lower crustal relaxation beneath the Tibetan Plateau and Qaidam Basin following the 2001 Kokoxili earthquake. *Geophysical Journal International*, *187*(2), 613–630. <https://doi.org/10.1111/j.1365-246X.2011.05179.x>
- Schiffman, C., Bali, B. S., Szeliga, W., & Bilham, R. (2013). Seismic slip deficit in the Kashmir Himalaya from GPS observations. *Geophysical Research Letters*, *40*, 5642–5645. <https://doi.org/10.1002/2013GL057700>
- Simons, W., Socquet, A., Vigny, C., Ambrosius, B., Haji Abu, S., Promthong, C., et al. (2007). A decade of GPS in Southeast Asia: Resolving Sundaland motion and boundaries. *Journal of Geophysical Research*, *112*, B06420. <https://doi.org/10.1029/2005JB003868>

- Socquet, A., Vigny, C., Chamot-Rooke, N., Simons, W., Rangin, C., & Ambrosius, B. (2006). India and Sunda plates motion and deformation along their boundary in Myanmar determined by GPS. *Journal of Geophysical Research*, *111*, B05406. <https://doi.org/10.1029/2005JB003877>
- Sreejith, K. M., Sunil, P. S., Agrawal, R., Saji, A. P., Ramesh, D. S., & Rajawat, A. S. (2016). Coseismic and early postseismic deformation due to the 25 April 2015, M_w 7.8 Gorkha, Nepal, earthquake from InSAR and GPS measurements. *Geophysical Research Letters*, *43*, 3160–3168. <https://doi.org/10.1002/2016GL067907>
- Steckler, M. S., Mondal, D. R., Akhter, S. H., Seeber, L., Feng, L., Gale, J., et al. (2016). Locked and loading megathrust linked to active subduction beneath the Indo-Burman Ranges. *Nature Geoscience*, *9*(8), 615–618. <https://doi.org/10.1038/ngeo2760>
- Stevens, V. L., & Avouac, J. P. (2015). Interseismic coupling on the main Himalayan thrust. *Geophysical Research Letters*, *42*, 5828–5837. <https://doi.org/10.1002/2015GL064845>
- Suito, H., & Freymueller, J. T. (2009). A viscoelastic and afterslip postseismic deformation model for the 1964 Alaska earthquake. *Journal of Geophysical Research*, *114*, B11404. <https://doi.org/10.1029/2008JB005954>
- Szeliga, W., Bilham, R., Kakar, D. M., & Lodi, S. H. (2012). Interseismic strain accumulation along the western boundary of the Indian subcontinent. *Journal of Geophysical Research*, *117*, B08404. <https://doi.org/10.1029/2011JB008822>
- Tang, F.-T., Song, J., Cao, Z.-Q., Deng, Z.-H., Wang, M., Xiao, G.-R., & Chen, W.-T. (2010). The movement characters of main faults around Eastern Himalayan Syntaxis revealed by the latest GPS data, Diqui Wuli Xuebao. *Chinese Journal of Geophysics*, *53*(9), 2119–2128.
- Thomas, M. Y., Avouac, J. P., & Lapusta, N. (2017). Rate-and-state friction properties of the Longitudinal Valley Fault from kinematic and dynamic modeling of seismic and aseismic slip. *Journal of Geophysical Research: Solid Earth*, *122*, 3115–3137. <https://doi.org/10.1002/2016JB013615>
- Tian, Z., Freymueller, J. T., & Yang, Z. (2020). Spatio-temporal variations of afterslip and viscoelastic relaxation following the Mw7.8 Gorkha (Nepal) earthquake. *Earth and Planetary Science Letters*, *532*, 116031. <https://doi.org/10.1016/j.epsl.2019.116031>
- Wang, C. Y., Chen, W. P., & Wang, L. P. (2013). Temperature beneath Tibet. *Earth and Planetary Science Letters*, *375*, 326–337. <https://doi.org/10.1016/j.epsl.2013.05.052>
- Wang, E., Meng, K., Su, Z., Meng, Q., Chu, J. J., Chen, Z., et al. (2014). Block rotation: Tectonic response of the Sichuan basin to the southeastward growth of the Tibetan Plateau along the Xianshuihe-Xiaojiang fault. *Tectonics*, *33*(5), 686–718. <https://doi.org/10.1002/2013tc003337>
- Wang, K., & Fialko, Y. (2018). Observations and modeling of coseismic and postseismic deformation due to the 2015 M_w 7.8 Gorkha (Nepal) earthquake. *Journal of Geophysical Research: Solid Earth*, *123*, 761–779. <https://doi.org/10.1002/2017JB014620>
- Weiss, J. R., Qiu, Q., Barbot, S., Wright, T. J., Foster, J. H., Saunders, A., et al. (2019). Illuminating subduction zone rheological properties in the wake of a giant earthquake. *Science Advances*, *5*, eaax6720. <https://doi.org/10.1126/sciadv.aax6720>
- Wimpenny, S., Copley, A., & Ingleby, T. (2017). Fault mechanics and post-seismic deformation at Bam, SE Iran. *Geophysical Journal International*, *209*(2), 1018–1035. <https://doi.org/10.1093/gji/ggx065>
- Wright, T. J., Elliott, J. R., Wang, H., & Ryder, I. (2013). Earthquake cycle deformation and the Moho: Implications for the rheology of continental lithosphere. *Tectonophysics*, *609*, 504–523. <https://doi.org/10.1016/j.tecto.2013.07.029>
- Yamada, M., Kandel, T., Tamaribuchi, K., & Ghosh, A. (2020). 3D fault structure inferred from a refined aftershock catalog for the 2015 Gorkha earthquake in Nepal. *Bulletin of the Seismological Society of America*, *110*(1), 26–37. <https://doi.org/10.1785/0120190075>
- Yang, S., Li, J., & Wang, Q. (2008). The deformation pattern and fault rate in the Tianshan Mountains inferred from GPS observations. *Science in China Series D: Earth Sciences*, *51*(8), 1064–1080. <https://doi.org/10.1007/s11430-008-0090-8>
- Zhao, B., Burgmann, R., Wang, D. Z., Tan, K., Du, R. L., & Zhang, R. (2017). Dominant controls of down-dip afterslip and viscous relaxation on the postseismic displacements following the M_w 7.9 Gorkha, Nepal, earthquake. *Journal of Geophysical Research: Solid Earth*, *122*, 8376–8401. <https://doi.org/10.1002/2017JB014366>
- Zubovich, A. V., Wang, X. Q., Scherbakov, Y. G., Schelochkov, G. G., Reilinger, R., Reigber, C., et al. (2010). GPS velocity field for the Tien Shan and surrounding regions. *Tectonics*, *29*, TC6014. <https://doi.org/10.1029/2010TC002772>